Enhancing Silicon Solar Cell Efficiency With Metal Nanoparticles

Antti Pennanen

February 11, 2009

UNIVERSITY OF JYVÄSKYLÄ
DEPARTMENT OF PHYSICS

Preface

The literature research on metal nanoparticle enhanced silicon solar cells and the writing of this masters thesis was conducted during June–November 2008, for an OSKE (Centre of Expertise Programme) project *Nano Solar Cell* at Department of Physics in University of Jyväskylä.

I want to thank Dr. Jouko Korppi-Tommola for providing me with this interesting subject for masters thesis and my supervisor Dr. Jussi Toppari for advice and guidance. I'd also like to thank the people involved in the *NanoSC* project; Dr. Mauno Harju from Jyväskylä Innovation, Elja Kallberg from the Nanoscience Center of University of Jyväskylä and Juha Kauppinen from Miktech. This has been a great opportunity to work with a subject that I'm truly interested in. My thanks also go to the people at Holvi (and the other Holvi-spirited people at the Physics Departement) for the intellectual conversations and fertile working environment. Especially warm thanks with love go to the folk of Ropeapina; I can't imagine how I could've coped without your insanely inspiring friendship! And last, I thank my parents and sister for all the support I've received during the years.

Jyväskylä, February 11, 2009

Antti Pennanen

Contents

Chapter 1

Introduction

The solar photovoltaics industry is a rapidly growing business, with value of $10 billion per year and annual growth of over 30% [1], which involves a great deal of research both in the industrial and academic level. Academic research is a key factor in developing applications for domestic enterprises, so that they would be able to compete in international markets. As photovoltaic technologies are just breaking through commercially, there is a good opportunity for domestic enterprises to take position on the edge of the solar photovoltaic industry.

Silicon is and has for long been the most widely used material for photovoltaic cells. In 2004, at least 94% of commercial photovoltaic devices shipped were manufactured of silicon [2]. The status of silicon as the dominant commercial photovoltaic material is due to it's abundancy in nature, stability, non-toxicity and well established refining and processing technologies [3]. Although commercial single crystalline silicon solar cells have high efficiencies [2], their high manufacturing costs prevent them from breaking through in the energy markets. The thin-film silicon solar cells [4, 5] are cheaper to manufacture, but their efficiencies are low compared to those achieved with single crystalline silicon wafer based cells [6]. Therefore, the trend in the photovoltaic research is to reach for even higher efficiencies and less material consuming cell designs.

One promising approach to achieve these goals, and to lower the price of solar produced electricity to a commercially competitive level, is the exploitation of optical properties of metal nanoparticles in photovoltaic cells. The purpose of this thesis is to provide an overview of the research conducted, until present day, on metal nanoparticles as means to improve silicon solar cell efficiency. The research was focused on silicon as photovoltaic material because of the already existing wide industry built around it; the knowledge, processes and materials are already commercially available; and it can provide a part of the solution for the acute need of renewable energy.

Chapter 2

Theory

2.1 Silicon solar cells

Solar cells are photoelectric devices that convert the energy of solar radiation directly into electrical energy. In semiconducting material photons can excite electrons from valence band into conduction band, thus creating free charge carriers. Under normal conditions, however, the electrons quickly relax back into ground state, i.e., *recombine*. In solar cells, electrical assymmetry is provided in order to drive the electrons away from the vicinity of their original state to prevent the relaxation. The energy of photons is thus transferred to the excited electrons, and the energy of the electrons creates a potential difference, which can be used to drive current through an external circuit. [7]

The most typical solar cell structure is a *pn* junction made of monocrystalline silicon (c-Si). The *pn* junction is fabricated by doping one part of the silicon n type and other part p type, i.e., in one part of the silicon impurity atoms are presented in order to increase density of electrons relative to holes and in other part to increase density of holes relative to electrons, respectively. When p and n type silicon are brought together, a *pn* junction is formed, through which electrons diffuse from n to p region and holes from p to n, until an equilibrium is reached. As a result of the majority carrier diffusion, a region of fixed charge forms near the junction region as the atoms are now ionized. This region is called the *depletion zone*, as it is depleted of majority charge carriers. The fixed charge of the ionized atoms creates an electric field, which prevents the majority carriers from diffusing through the junction region, and thus provides the separation of the photogenerated charge carriers at the vicinity of the junction. The current generated by the photoexcited charge carriers is called *photocurrent*. [7]

The standard solar irradiance spectrum against which the performance of solar photovoltaic devices is measured, is the *Air Mass* 1.5 or AM1.5 spectrum. It
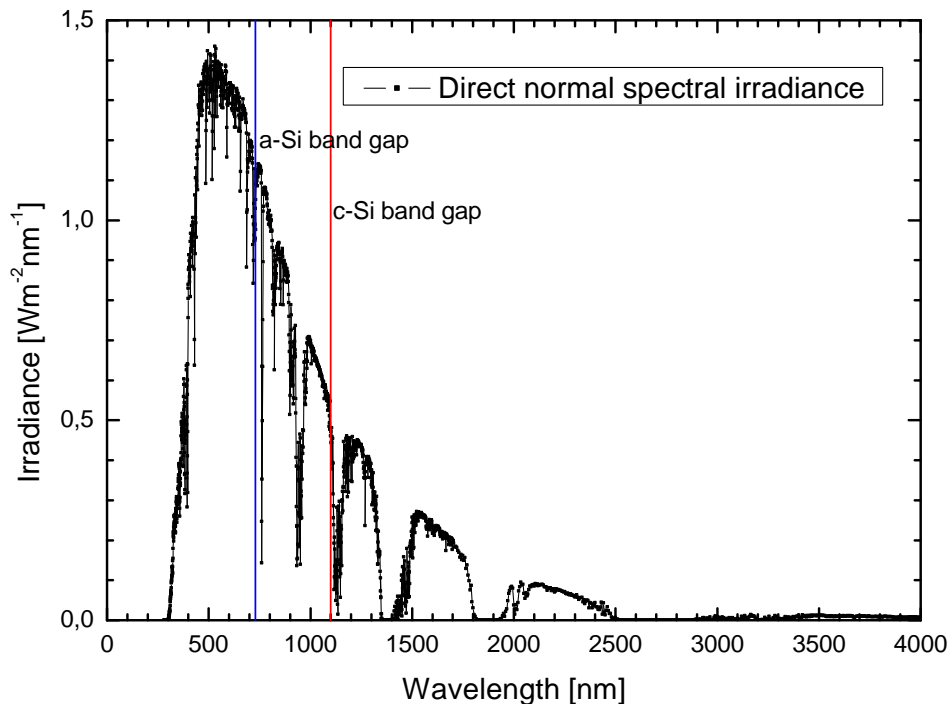
Figure 2.1: The Air Mass 1.5 solar irradiance spectrum and band gaps of crystalline and amorphous silicon. (Data for AM1.5 spectrum taken from ref. [9].

represents the solar irradiation attenuated by the earths athmosphere with sun at 42° angle of elevation [7]. The standard AM1.5 spectrum is presented in fig. 2.1. The vertical lines represent the band gaps of crystalline and amorphous silicon. Optical absorption occurs at photon energies exceeding the band gap energy, i.e., at wavelengths below the band gap wavelength. In silicon solar cells, absorption is weak at energies near the band gap, and gets stronger with higher photon energies, i.e., lower wavelengths. However, at short wavelengths the photocurrent is decreased, because the highest energy photons are absorbed near the cell surface, at which the *surface recombination*[1] is high [8].

---

1. Recombination of charge carriers due to the defects near a crystal surface [7].

2.1.1 Single crystalline silicon solar cells

Single crystalline or monocrystalline silicon (c-Si) consists of single silicon crystal. The band gap energy of c-Si is good for efficient absorption of a large part of the solar irradiance spectrum, as evident from. fig. 2.1. This means that the maximum efficiency of a single crystalline silicon photovoltaic cell is high (26.2% under AM1.5 spectrum [10]). The actual efficiencies of single crystalline silicon cells come within few percent of this limiting efficiency [2, 6, 10], and there are even commercial single crystalline silicon solar cells that have demonstrated efficiencies exceeding 20% [2].

The main drawback of single crystalline silicon is it's low optical absorption coefficient, especially at photon energies near the band gap, i.e., at near infrared wavelengths. This is due to the fact that crystalline silicon is an indirect band gap material, meaning that the maximum of the valence band energy and minimum of the conduction band energy occur at different values of wave vector **k**. This means that for an electron to be excited from valence to conduction band, an exchange of momentum is needed in addition to exchange of energy with a photon. As photons carry virtually no momentum, the exchange has to be conducted with a phonon instead, and the probability of electron excitation is decreased (compared to direct band gap materials), especially at lower photon energies. Because of the weak optical absorption in crystalline silicon, c-Si solar cells must be made thick and/or efficient means of light trapping must be utilized. [7]

2.1.2 Thin-film silicon solar cells

Because of the high manufacturing costs of high quality single crystalline silicon wafers (although cheap compared to those of other single crystalline semiconductor materials used in photovoltaic devices, such as gallium-arsenide) there has been a growing interest in developing alternative materials for photovoltaics. The most promising of these are the thin-film silicon materials [4], which can be divided into two sub-categories: amorphous silicon (a-Si) and crystalline silicon thin-films. Crystalline silicon thin-film materials include microcrystalline (μc-Si) and polycrystalline (poly-Si) silicon [11]. The key properties of thin-film solar cell materials are low cost and more efficient absorption than in bulk single crystalline silicon, which reduces the required cell thickness. [7]

Amorphous silicon does not posses the organized crystal structure of crystalline silicon. This leads to relaxed conditions for photon absorption. Therefore, amorphous silicon has better absorption coefficient than crystalline sili-

con, as can be seen from fig. 2.2. The band gap of amorphous silicon is, however, at higher energy than that of crystalline silicon. The unorganized structure of amorphous silicon also shows as a high density of defects, which shortens the charge carrier diffusion lengths and decreases the doping efficiency. Because of the short charge carrier diffusion lengths, the amorphous silicon solar cells typically have *p-i-n* junction structure, where wide region of undoped intrinsic silicon is left between the p and n doped regions. The function of the intrinsic region is to increase the width of the depletion zone, i.e., the area in which the photogenerated carriers are separated. [7]

Micro- and polycrystalline silicon both consist of grains of crystalline silicon. They have the organized crystal structure within the grains, but the order is broken at the grain boundaries. In μc-Si the grain size is smaller than one micron, whereas in poly-Si it is much larger [11]. The charge carrier transfer and recombination properties of micro- and polycrystalline silicon are mostly determined by the grain boundary effects [7].

Due to the short carrier diffusion lengths, the thickness of a thin-film silicon solar cell must be kept as small as possible. This emphasizes the importance of efficient light trapping. However, for thin-films, the conventional method of light-trapping by surface texturing is problematic. Features of these surface textures typically have depths in the range of tens of microns [12], i.e., more than the thickness of a thin-film photovoltaic device, which can be as little as one micron [5]. Furthermore, plasma etch techniques capable of crafting features less than a micron scale can damage the silicon and thus reduce the cell efficiency [3]. Instead of texturing the silicon, the substrate upon which the silicon film is grown can be textured, but this presents problems with increased surface recombination due to increased surface area [3].
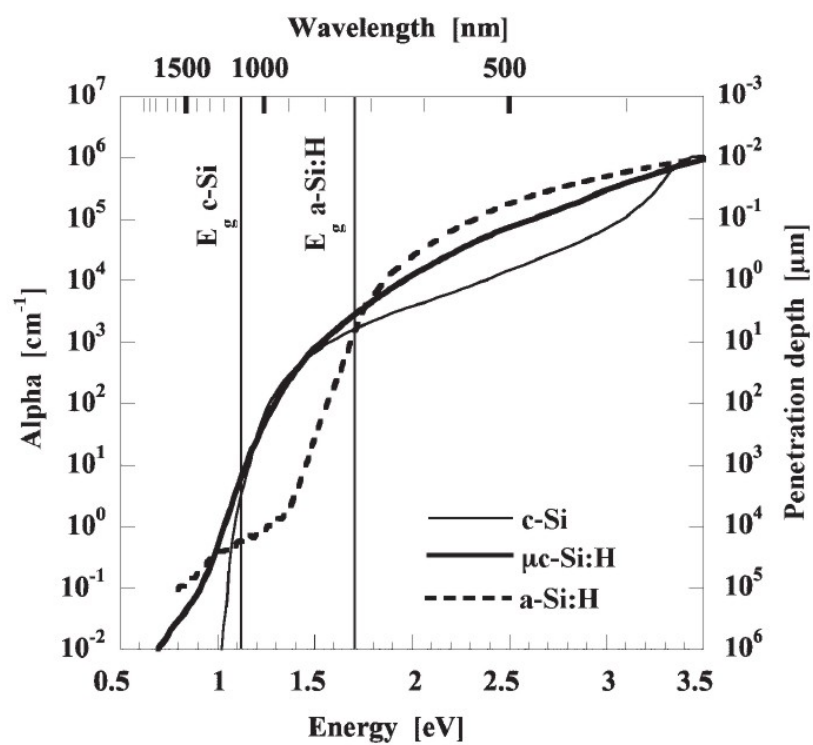
Figure 2.2: Optical absorption coefficient and penetration depth for electromagnetic radiation in single crystalline, microcrystalline and amorphous silicon [5].

2.2 Absorption and scattering of light

Electric field of electromagnetic radiation incident on an object induces oscillations of electric charges in that object. The charges in accelerating motion then radiate an electric field in all directions; this is called *scattering* [13]. However, the excited electric charges may not reradiate all of the incident electromagnetic energy; this electromagnetic energy that takes part in excitation of the particle but is not reradiated is referred to as *absorption* [13]. This energy is transferred to other forms, such as thermal energy or stored in local, non-radiative fields near the object (the near field).

When an object is placed within a beam of electromagnetic radiation, a detector that is deviated from the direction of propagation of the incident radiation will only perceive the radiation scattered by the object. A detector placed within the beam "downstream" from the object will detect that part of the beam which remains unaffected by the object. This part of the incident electromagnetic radiation is called *transmitted* radiation, and if the transmitted energy is less than the energy incident on the object, it is said that the object has caused *extinction* of the electromagnetic radiation [13]. The energy that is not radiated, i.e., the difference between incident energy and sum of transmitted and scattered energies, is accounted for by the absorption. Therefore, extinction is the sum of absorption and scattering. (See fig. 2.3.)

These definitions are macroscopic in nature; scattering is comprised of (radiative) electromagnetic fields observed "far" away from the object by a detector that is deviated from the direction of propagation of the incident radiation, and absorption accounts for the energy removed from the radiative (i.e., scattered and transmitted) fields. However, when we investigate extinction of electromagnetic radiation at distances comparable to the wavelength of the radiation, distinguishing between transmitted, absorbed and scattered fields becomes difficult (we are within the boundaries of the dashed line in fig. 2.3). Even if we can theoretically separate these, by separation into radiative and non-radiative fields, we can only observe the total field, which is the sum of the aforementioned fields, and the distinction becomes artificial. Thus, when we speak of *scattering* within this thesis, we often actually mean absorption as well. This is due to nomenclature used in the articles discussed within this thesis, and the nomenclature is originally developed for macroscopic optics.
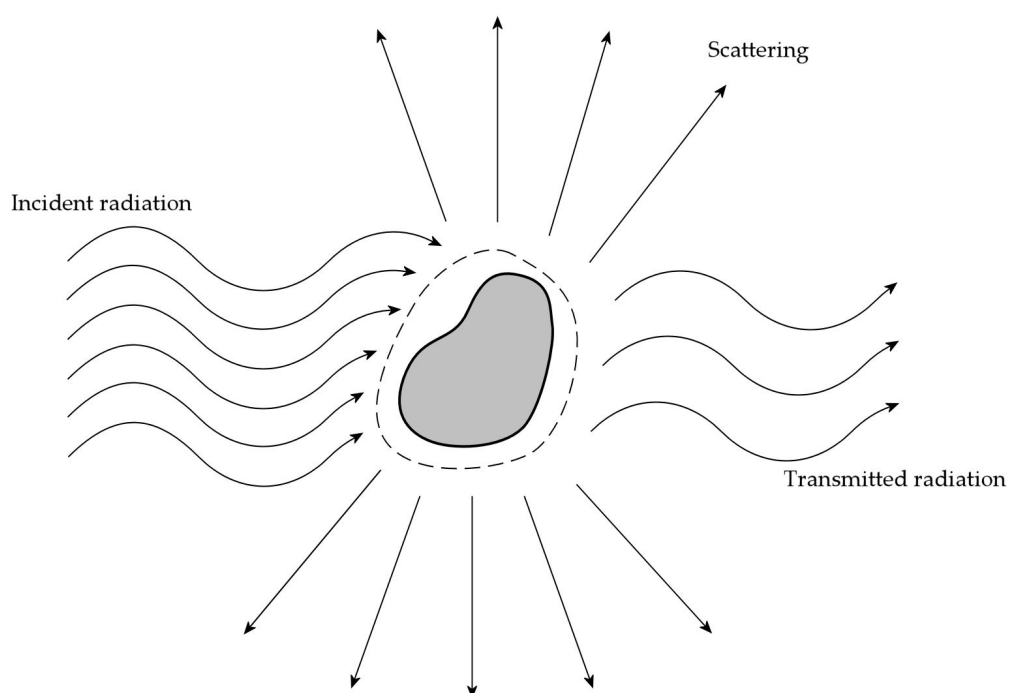
Figure 2.3: Absorption and scattering of light by an arbitrary particle. A detector deflected from the path of the incident radiation far away from the particle detects only the scattered field. The incident radiation that is not scattered or transmitted by the particle, i.e., the energy that is confined within the boundaries of the dashed line in the figure, accounts for absorption.

2.3 Plasmons

The structure of metals can be understood as a gas of free electrons in a lattice of positively charged ions. Let's consider the electron gas in equilibrium; everywhere in the metal lattice there is equal amount of negative and positive charge, and the net charge density is zero. However, if the system is disturbed from equilibrium there will be a local non-zero net charge density, and an internal electric field is created in order for the system to retain charge neutrality. As the mass of the metal ions is significantly larger than the mass of the electrons, the electrons are considered to move against a background of fixed ion lattice. The electrons will acquire momentum from the field, and thus begin oscillating around their equilibrium position. This collective, longitudial oscillation of a *plasma* – of which the free electron gas in metal is an example – is called a *plasma wave*. The quantization of these plasma waves is the *plasmon*.

2.3.1 Bulk plasmons

The plasmons in an unbounded plasma – such as in an infinite metal lattice, as in the example above – are *bulk plasmons*. The natural frequency of plasma oscillations in unbounded plasma is referred to as *plasma frequency*. The plasma frequency of free-electron gas is[14, 15]

$$\omega_p = \sqrt{\frac{ne^2}{\varepsilon_0 m}},\qquad(2.1)$$

where e and m are the charge and effective optical mass of electron, ε_0 the permittivity of free space and n the electron density. Impinging electromagnetic radiation with frequency near the plasma frequency can induce resonance, strengthening the plasma oscillations – a phenomenon referred to as the *plasmon resonance*. Because of their large number of free-electrons, i.e., large n in eq.(2.1), the plasmon resonance of metals occurs at optical frequencies [12], which makes metal nanoparticles particularly interesting considering solar cell applications.

The electromagnetic properties of metals are described by a complex, frequency dependent dielectric function $\varepsilon(\omega)$, which can be written in general form

$$\varepsilon(\omega) = \varepsilon_1(\omega) + i\varepsilon_2(\omega),\qquad(2.2)$$

where ω is the angular frequency of the electromagnetic radiation. The imaginary part $\varepsilon_2(\omega)$ of this dielectric function determines the amount of absorption

of the radiation in the material, whereas the real part $\varepsilon_1(\omega)$ correlates to the lowering of the phase velocity of the wave, due to polarization in the metal [15]. In the *plasma model* for metals, which is qualitatively described above, the values of the imaginary and real parts of the dielectric function depend on the collision frequency of the electrons. The dielectric function of an undamped free-electron gas – i.e., electron gas with negligible collision frequency – is real, and simplifies to [15]

$$\varepsilon(\omega) = 1 - \frac{\omega_p^2}{\omega^2}. \tag{2.3}$$

A metal with electron structure of free-electron gas is called a *Drude metal*, and is described by dielectric function (2.3). It should, however, be noted that the Drude model of metals is only an idealization and describes none of the real metals perfectly. The plasma model of metals is valid over frequency range up to the ultraviolet for alkali metals and to visible frequencies for noble metals [15], where interband transitions of electrons begin to occur. The plasma model yields the dispersion relation for a Drude metal as [15]

$$\omega^2 = \omega_p^2 + \mathbf{K}^2 c^2, \tag{2.4}$$

where $\mathbf{K}$ is the wave vector and c the speed of light in vacuum. The dispersion relation is plotted in fig. 2.4. From the dispersion curve it can be seen, that inside a plasma, propagating transverse electromagnetic waves are allowed only for frequencies $\omega > \omega_p$. The group velocity for propagating waves is given by $v_g = \mathrm{d}\omega/\mathrm{d}\mathbf{K}$. For $\omega = \omega_p$ the wavevector $\mathbf{K}$ is zero, as is the group velocity, and thus ω_p corresponds to a collective longitudial oscillation, which is the bulk plasmon.
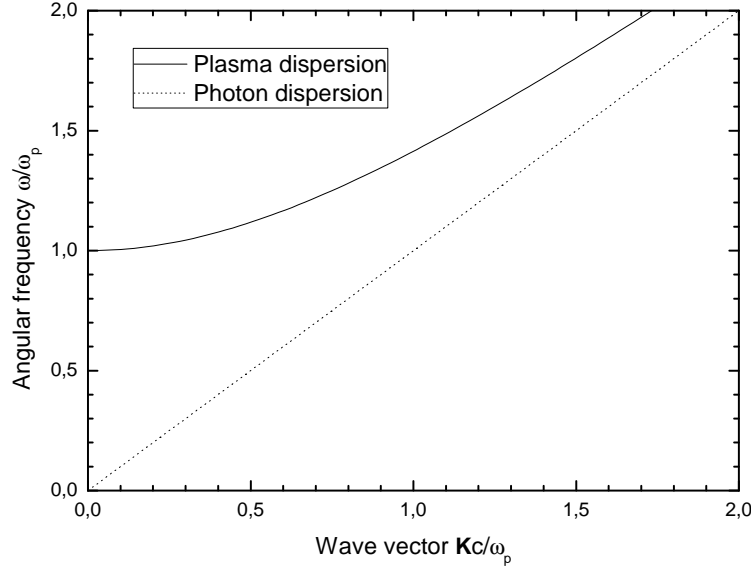
Figure 2.4: Dispersion of free electron gas.

2.3.2 Surface Plasmons

As the plasma oscillation is caused by long-range Coulomb interactions of electrons, the nature of these oscillations is different in the presence of boundaries limiting the movement of electrons. Plasma oscillations confined to a conductor surface in a conductor-insulator interface are called *surface plasmon polaritons* or SPPs. They originate from coupling of electromagnetic radiation to electron plasma excitations propagating along the interface, and they only exist on interfaces between materials with real parts of their dielectric permittivities of opposite signs – i.e., in interfaces between a conductor and an insulator.

The surface plasmon polaritons can be derived quantitatively from the solutions of the electromagnetic wave equation at an interface between a dielectric, non-absorbing material with positive dielectric constant ε_1 and a conducting material with dielectric function $\varepsilon(\omega)$ [15, 16]. Due to the confinement to the interface, the component of the electric field normal to the interface is evanescent, and decreases exponentially with increasing distance from the interface. The electric field of a surface plasmon polariton in a metal-insulator interface, obtained from the solution of the wave equation derived in [15], is depicted in
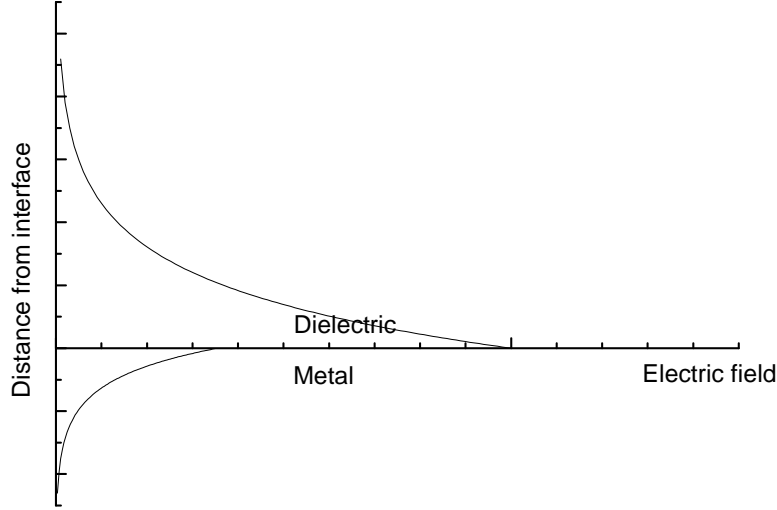
Figure 2.5: The electric field of a surface plasmon polariton in a dielectric-metal interface.

fig. 2.5.

The SPPs only exist for transverse magnetic (TM) polarization, i.e., the magnetic field of the SPP only has a component perpendicular to the direction of propagation. The solution to the wave equation also yields the dispersion relation for the SPPs [15],

$$\beta = k_0 \sqrt{\frac{\varepsilon(\omega)\varepsilon_1}{\varepsilon(\omega) + \varepsilon_1}}. \tag{2.5}$$

Here β is the component of the wave vector in direction of propagation of the plasma oscillation at the interface, $k_0 = \omega/c$ the wave number of radiation in vacuum, and ε and ε_1 the dielectric permittivities of the conductor and insulator, respectively. The dispersion of SPPs at an interface between Drude metal and air is depicted in fig. 2.6. Both real and imaginary parts of the wave vector β of the propagating plasma wave are shown.

The lower branch of the dispersion curve represents the SPP mode. It can be observed that in the limit of wave vector β approaching infinity, the group velocity $v_g = \mathrm{d}\omega/\mathrm{d}\beta$ becomes zero and the angular frequency approaches a finite value, called the *surface plasmon frequency* [15],
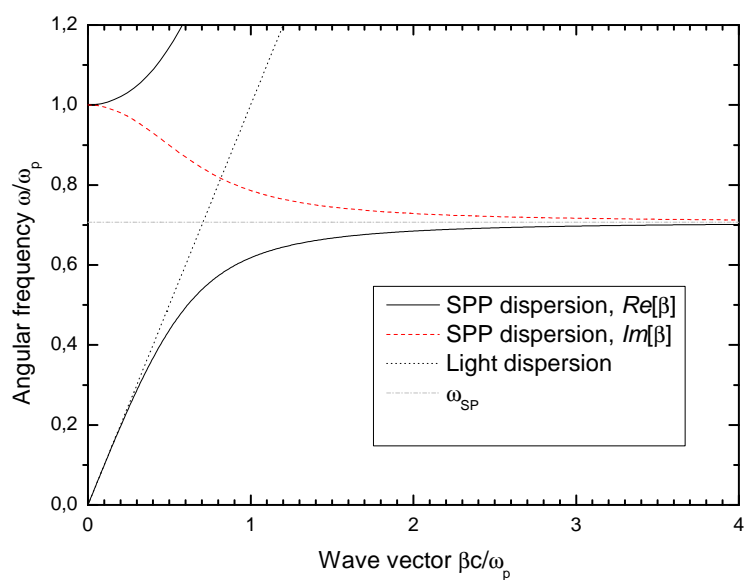
Figure 2.6: Dispersion of surface plasmon polaritons in interface between Drude metal and air.
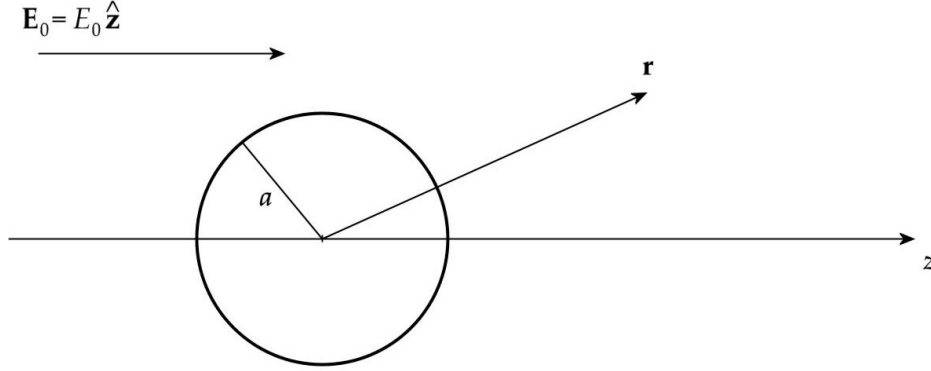
Figure 2.7: A spherical particle in a uniform electric field.

$$\omega_{sp} = \frac{\omega_p}{\sqrt{1 + \varepsilon_1}}. \qquad (2.6)$$

This corresponds to a special case of SPP, a non-propagating surface excitation, known as *surface plasmon*. The upper branch, however, approaches a finite group velocity with increasing wave vector β, and thus corresponds to a radiative mode [15]. Also, there is a region of purely imaginary wave vector between ω_{sp} and ω_p, in which the plasma propagation is prohibited, and which separates the bound and radiative modes. Note that we consider here only an ideal drude metal; for real metals, there is a *quasibound* region in the dispersion relation between ω_{sp} and ω_p, which is now allowed [15].

2.3.3 Localized surface plasmons on metal nanoparticles

The third type of plasmons is the *localized surface plasmon*, or LSP for short. Localized surface plasmons are non-propagating plasma oscillations that occur in the electron gas of metallic nanoparticles, much smaller than the wavelength of the exciting electromagnetic wave. The LSP can be thought of as a combination of properties of both bulk and surface plasmons; as the electron "cloud" of a metallic nanoparticle is disturbed from its state of equilibrium by an external field, net charges with opposite signs are created on opposing sides of the particle, creating an electric field, reverse to the exciting field, and resulting in a restoring force. In case of an oscillating incident electric field with suitable frequency, the restoring force enables resonant oscillations of electron plasma, called the localized surface plasmon resonance.

The properties of localized surface plasmons on metal nanoparticles can be examined analytically through straightforward electrostatic approach. In order to do that, let's consider a spherical particle with permittivity ε and radius a, in surrounding dielectric medium with permittivity ε_m, in a static, uniform electric field $\mathbf{E}_0 = E_0\hat{z}$. The geometry of the problem is depicted in fig. 2.7, with the sphere located at the origin of spherical coordinates. The subject we are interested in is the extinction in the sphere. In order to investigate this, we first need to find out the electric field in the presence of the particle. This is done by solving the *Laplace equation* for electric potential, inside and outside the sphere;

$$\nabla^2\Phi_{in} = 0, \ r < a \tag{2.7}$$
$$\nabla^2\Phi_{out} = 0, \ r > a. \tag{2.8}$$

Due to the symmetry in respect to azimuth angle φ, the solutions to the equations above are of form [15]

$$\Phi = \Phi(r, \theta) = \sum_0^{l=\infty} [A_l r^l + B_l r^{-(l+1)}]P_l(\cos\theta), \tag{2.9}$$

where A_l and B_l are real constants and P_l the *Legendre* polynomials of lth degree. The requirement that the potential remains finite at the origin results in that the potential inside the sphere is

$$\Phi_{in}(r, \theta) = \sum_0^{l=\infty} A_l r^l P_l(\cos\theta), \tag{2.10}$$

whereas the potential outside the sphere remains as

$$\Phi_{out}(r, \theta) = \sum_0^{l=\infty} [B_l r^l + C_l r^{-(l+1)}]P_l(\cos\theta), \tag{2.11}$$

where C_l is also a real constant. If we further require that $\mathbf{E}_{out}(r \to \infty) = \mathbf{E_0}$, i.e., the electric field remains unperturbed far away from the sphere, we get

$$\lim_{r\to\infty} \Phi_{out}(r, \theta) = \sum_0^{l=\infty} B_l r^l P_l(\cos\theta) = E_0 z = -E_0 r \cos\theta, \tag{2.12}$$

which gives the coefficients B_l as $B_1 = -E_0$ and $B_l = 0$ for $l \neq 1$ [13]. The continuity of the electric potential and the normal component of electric displacement field $\mathbf{D}$ at the surface of the sphere require that

$$\Phi_{in}(r = a) = \Phi_{out}(r = a) \tag{2.13}$$

and

$$\varepsilon \frac{\partial \Phi_{in}}{\partial r}\bigg|_{r=a} = \varepsilon_m \frac{\partial \Phi_{out}}{\partial r}\bigg|_{r=a}. \tag{2.14}$$

If we limit ourselves to the first order approximation, i.e., take into consideration only the two first terms in the sum, eqns. (2.13) and (2.14) yield

$$-E_0 a \cos\theta + C_0 a^{-1} + C_1 a^{-2} \cos\theta = A_0 + A_1 r \cos\theta \tag{2.15}$$

and

$$\varepsilon A_1 \cos\theta = -\varepsilon_m E_0 \cos\theta - \varepsilon_m C_0 a^{-2} - 2\varepsilon_m C_1 a^{-3} \cos\theta, \tag{2.16}$$

respectively. Combining eqns. (2.15) and (2.16) gives the solutions for coefficients A_l and C_l as

$$A_0 = 0 = C_0 \tag{2.17}$$

$$A_1 = -\frac{3\varepsilon_m}{\varepsilon + 2\varepsilon_m} E_0 \tag{2.18}$$

$$C_1 = \frac{\varepsilon - \varepsilon_m}{\varepsilon + 2\varepsilon_m} a^3 E_0. \tag{2.19}$$

Substituting these into eqns. (2.10) and (2.11) yields the electric potentials inside and outside the sphere as [13, 15]

$$\Phi_{in} = -\frac{3\varepsilon_m}{\varepsilon + 2\varepsilon_m} E_0 r \cos\theta \tag{2.20}$$

and

$$\Phi_{out} = -E_0 r \cos\theta + \frac{\varepsilon - \varepsilon_m}{\varepsilon + 2\varepsilon_m} a^3 E_0 \frac{\cos\theta}{r^2}, \tag{2.21}$$

which one can easily see to satisfy all the boundary conditions stated above.

It is illustrative to compare the equation (2.21) of the potential outside the sphere to that of an ideal point dipole in medium with permittivity ε_m, given by

$$\Phi_{dip} = \frac{\mathbf{p} \cdot \mathbf{r}}{4\pi\varepsilon_0\varepsilon_m r^3}, \tag{2.22}$$

where $\mathbf{p}$ is the *dipole moment*. Now, by writing [15]

$$\mathbf{p} = 4\pi\varepsilon_0\varepsilon_m a^3 \frac{\varepsilon - \varepsilon_m}{\varepsilon + 2\varepsilon_m} \mathbf{E}_0, \tag{2.23}$$

we can rewrite equation (2.21) for potential outside the sphere as [15]

$$\Phi_{out} = -E_0 r \cos\theta + \frac{\mathbf{p} \cdot \mathbf{r}}{4\pi\varepsilon_0\varepsilon_m r^3}, \tag{2.24}$$

from which we can observe that the electric potential outside the sphere is the sum of the original potential and the potential of an ideal dipole, i.e., the applied electric field induces a dipole moment in the sphere, proportional to the original field [13].

The *polarizability*, denoted by α, describes how easily a particle is polarized, and is defined by

$$\mathbf{p} = \varepsilon_0\varepsilon_m\alpha\mathbf{E}_0. \tag{2.25}$$

The polarizability of a metallic sphere is then obtained from equation (2.24) as [13, 15]

$$\alpha = 4\pi a^3 \frac{\varepsilon - \varepsilon_m}{\varepsilon + 2\varepsilon_m}. \tag{2.26}$$

Electric field can be obtained from the electric potential with $\mathbf{E} = -\nabla\Phi$, which gives the electric field outside the sphere as

$$\mathbf{E}_{out} = -\nabla\Phi_{out} = E_0 \cos\theta(1 + \frac{2}{4\pi r^3})\hat{\mathbf{r}} + E_0 \sin\theta(\frac{1}{4\pi r^3} - 1)\hat{\theta}, \tag{2.27}$$

which in turn simplifies to [15]

$$\mathbf{E}_{out} = \mathbf{E}_0 + \frac{3(\hat{\mathbf{r}} \cdot \mathbf{p})\hat{\mathbf{r}} - \mathbf{p}}{4\pi\varepsilon_0\varepsilon_m r^3}. \tag{2.28}$$

All of the results above were derived assuming a sphere in a static electric field. However, we now embark on describing the extinction of electromagnetic radiation by spherical particle by assuming that the particle may still be described as an ideal dipole even when the incident electric field is a plane wave. We may approximate that the particle resides in a uniform electric field, if the amplitude of the incident electric field is constant over the sphere. This is valid for a particle with diameter much smaller than the wavelength of the incident electromagnetic wave. This is called the *electrostatic approximation* [13, 15]. Electric field of plane wave radiation over the particle, $\mathbf{E}_0(\mathbf{r}, t) = \mathbf{E}_0 e^{-i\omega t}$, induces an oscillating dipole moment

$$\mathbf{p}(t) = \varepsilon_0\varepsilon_m\alpha(\omega)\mathbf{E}_0 e^{-i\omega t} \tag{2.29}$$

in the sphere [13, 15]. Here the polarizability $\alpha(\omega)$ of a sub-wavelength spherical particle is obtained from eq. (2.26) by replacing ε with the angular frequency dependent dielectric function $\varepsilon(\omega)$. The electric field of an oscillating electric dipole is [15]

$$\mathbf{E} = \frac{1}{4\pi\varepsilon_0\varepsilon_m} \left\{ \frac{k^2 e^{ikr}}{r}(\hat{\mathbf{r}} \times \mathbf{p}) \times \hat{\mathbf{r}} + \left(\frac{1}{r^3} - \frac{ik}{r^2} \right) e^{ikr}[3(\hat{\mathbf{r}} \cdot \mathbf{p})\hat{\mathbf{r}} - \mathbf{p}] \right\}, \tag{2.30}$$

and we now assume that this is the electric field outside the particle. Eq. (2.30) contains three terms distinguishable by their dependence on distance r from the dipole. Here, $k = 2\pi/\lambda$ is the wave number, where λ denotes the wavelength, as usual. In the immediate vicinity of the dipole, where $kr \ll 1$, the $1/r^3$ term dominates, giving the *near field* of the oscillating dipole as

$$\mathbf{E}_{near} = \frac{3(\hat{\mathbf{r}} \cdot \mathbf{p})\hat{\mathbf{r}} - \mathbf{p}}{4\pi\varepsilon_0\varepsilon_m r^3}, \tag{2.31}$$

which is a non-propagating oscillatory field (note that $\mathbf{p}$ contains the time-dependent $e^{-i\omega t}$ -term), similar to the electrostatic field of eq. 2.28. Far away from the dipole, where $kr \gg 1$, term with e^{ikr}/r dominates, giving the *far field* of the dipole as

$$\mathbf{E}_s = \frac{k^2 e^{ikr}}{4\pi\varepsilon_0\varepsilon_m r}(\hat{\mathbf{r}} \times \mathbf{p}) \times \hat{\mathbf{r}}, \tag{2.32}$$

which is a propagating spherical wave. This is now the radiative part of the electric field of the oscillating dipole, i.e., the scattered field (hence the subscript s). Apart from these two terms that dominate at opposing limits of large and small r, the electric field of an oscillating dipole contains a third term proportional to ike^{ikr}/r^2. This part of the electric field is purely imaginary, and not observable.

The scattered field (2.32) may be rewritten in form

$$\mathbf{E}_s = \frac{e^{ikr}}{-ikr}\mathbf{X}E_0, \tag{2.33}$$

where

$$\mathbf{X} = \frac{ik^3}{4\pi}\alpha(\hat{\mathbf{r}} \times \mathbf{p}) \times \hat{\mathbf{r}} \tag{2.34}$$

is the vector scattering amplitude [13]. We shall omit the details here, but the scattering and absorption cross sections can be obtained from expression (2.34) by solving scalar amplitude scattering matrix elements [13]. This yields the scattering and absorption cross sections of a spherical particle in the electrostatic dipolar approximation as [13, 15]

$$C_{sca} = \frac{k^4}{6\pi}|\alpha|^2 = \frac{4(2\pi)^5 a^6}{3\lambda^4}\left|\frac{\varepsilon - \varepsilon_m}{\varepsilon + 2\varepsilon_m}\right|^2 \tag{2.35}$$

and

$$C_{abs} = k\mathrm{Im}(\alpha) = \frac{8\pi^2 a^3}{\lambda}\mathrm{Im}\left(\frac{\varepsilon - \varepsilon_m}{\varepsilon + 2\varepsilon_m}\right). \tag{2.36}$$

It should be noted that we have come to these results by *assuming*, that the electric field of a spherical particle may be described as a field created by an electric dipole, even when the exciting field is a plane wave, although we only have shown this to be true for a static field. However, excactly same expressions for absorption and scattering cross sections for a sub-wavelength particle may also be obtained from electrodynamic theory of scattering and absoroption of electromagnetic radiation by a spherical particle, known as the

Mie theory. This theory contains a complete electrodynamic treatment of the problem by series expansion of electric fields inside and outside the particle, and the results of electrostatic approximation are obtained by including only the first order terms [13, 15]. We will exclude the details here, and adhere to noting that correct expressions for scattering and absorption cross sections for a sub-wavelength particle are obtained from staightforward electrostatic approximation, presented above. Scattering problem of an ellipsoid particle may also be treated in similar manner, with both the electrostatic approximation and Mie theory. In case of an ellipsoid particle, this yields different polarizabilities for each principal axis of the ellipsoid [13, 15]. Cross sections obtained from eqs. (2.35) and (2.36) as function of wavelength, for 50 and 100 nm diameter spherical particles of silver, gold and copper, are plotted in figs. 2.8, 2.9 and 2.10, respectively, with data of dielectric functions taken from ref. [17]. Through scattering and absorption cross sections we may also define the *radiative efficiency* as $C_{sca}/(C_{sca} + C_{abs})$. Considering scattering and absorption as the only mechanisms of plasmon relaxation, the radiative efficiency indicates how large portion of the plasmon energy is reradiated by the particle. Radiative efficiencies for 50 and 100 nm diameter spherical particles of silver, gold and copper, are shown in fig. 2.11.

From eq. (2.30) it can be seen that the electric field of the particle is directly proportional to the polarization **p**. Now, if the denominator in the expression (2.26) for polarizability α was zero for some angular frequency ω of incident electromagnetic wave, the polarization – and in turn the electric field – of the particle would become indefinitely large. This occurs when $|\varepsilon(\omega) + 2\varepsilon_m| = 0$ which for a metal with predominantly real $\varepsilon(\omega)$ simplifies to

$$\mathrm{Re}(\varepsilon(\omega)) = -2\varepsilon_m, \tag{2.37}$$

which is called the *Fröhlich condition*. In case of an undamped Drude metal, this condition is met at frequency (note the slight difference to eq. 2.6)

$$\omega_{lsp} = \frac{\omega_p}{\sqrt{1 + 2\varepsilon_m}}. \tag{2.38}$$

The plasma oscillation mode associated to this resonance frequency is known as the localized surface plasmon. In fig. 2.8, resonant enhancement of scattering and absorption cross sections of silver particles is observed near 350 nm wavelength. This is caused by the resonant enhancement in polarizability of the particle near its LSP frequency.
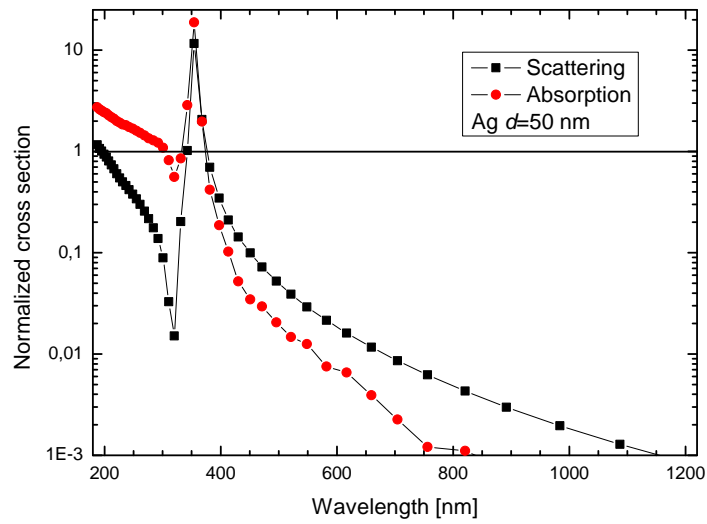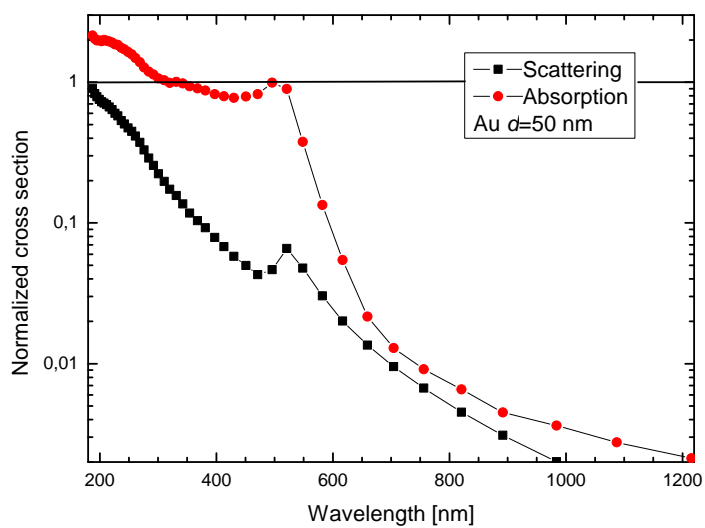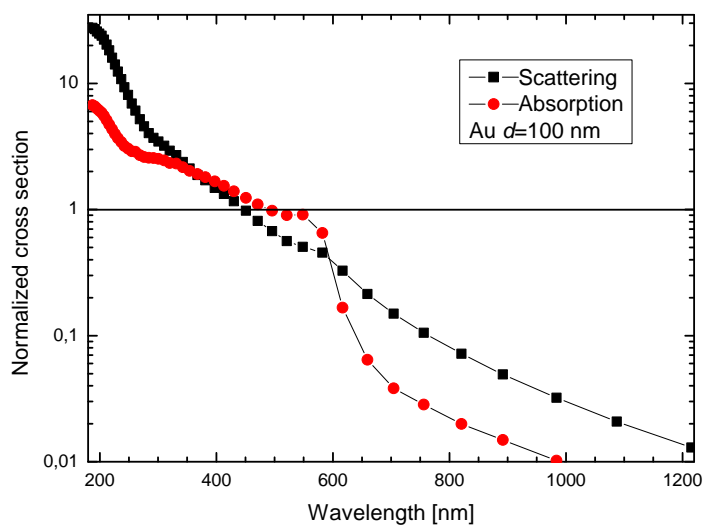
(a)
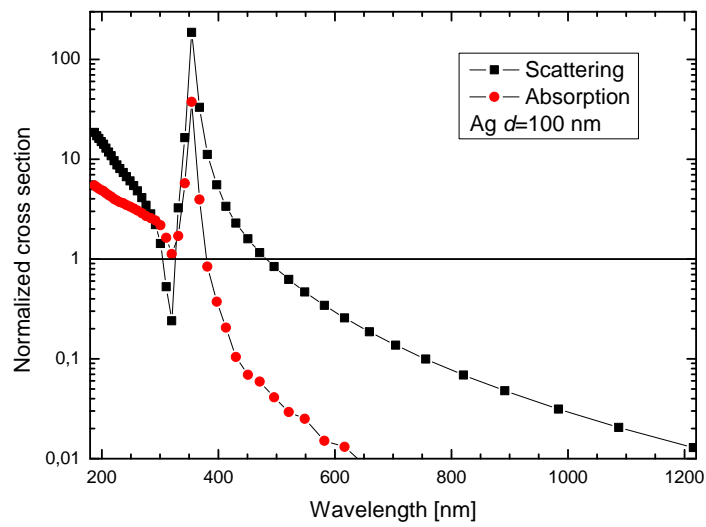
(b)

Figure 2.8: Absorption and scattering cross sections for a silver sphere of 50 nm (a) and 100 nm (b) diameter in air, with the dielectric data taken from ref. [17].
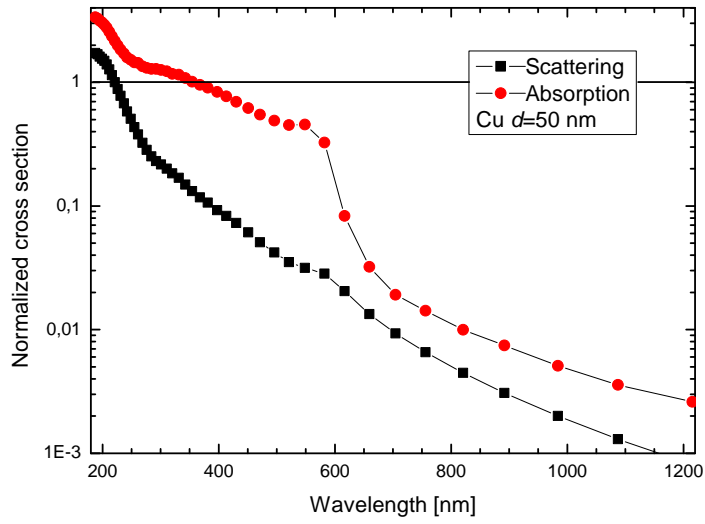
(a)

(b)

Figure 2.9: Absorption and scattering cross sections for a gold sphere of 50 nm (a) and 100 nm (b) diameter in air, with the dielectric data taken from ref. [17].

(a)

(b)

Figure 2.10: Absorption and scattering cross sections for a copper sphere of 50 nm (a) and 100 nm (b) diameter in air, with the dielectric data taken from ref. [17].
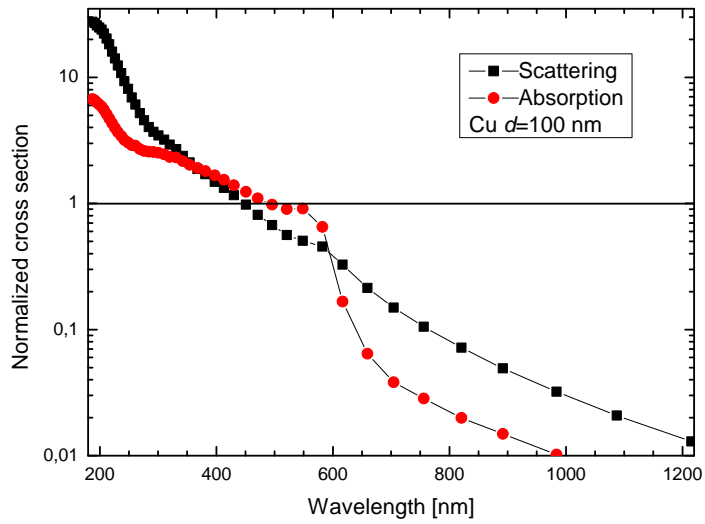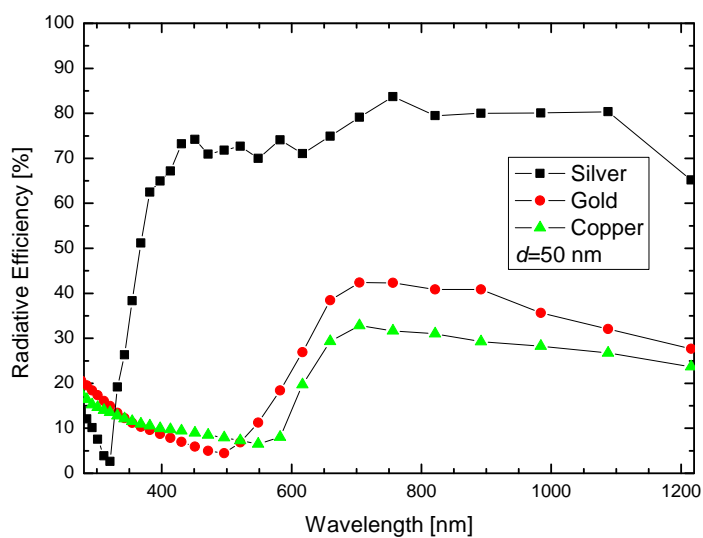
(a)
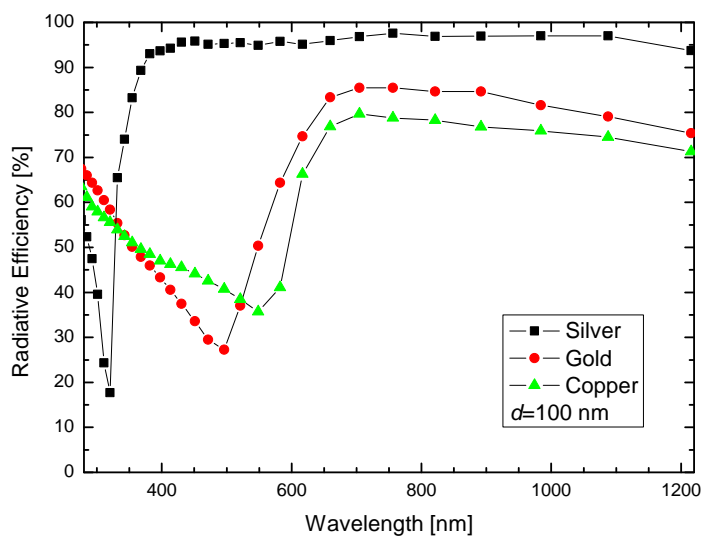
(b)

Figure 2.11: Radiative efficiency for silver, gold and copper nanoparticles of 50 nm (a) and 100 nm (b) diameter in air, with the dielectric data taken from ref. [17].

Relations derived above only describe the dipolar surface plasmon modes on metal nanoparticles. However, excitation of multipole oscillations is also possible, e.g. in case of irregular particle shape and/or non-uniformity of the electric field over the particle – i.e., exceeding the sub-wavelength size constraint. In latter case, correct expressions for scattering and absorption cross sections can be obtained from the Mie theory, by including sufficient amount of higher order terms into analysis. Non-spherical particles are out of grasp of the Mie theory.

Chapter 3

Previous studies

In this chapter we will take a look on the previously published studies concerning photovoltaic applications of localized surface plasmons on metal nanoparticles. These studies will include, beside those directly concerning solar cell applications, also investigations into silicon based light emitting diodes (LEDs) and photodetectors. The main subject of interest in the studies concerning photodetectors is the improvement of photosensitivity, but the mechanism through which this is achieved, i.e., enhanced photoabsorption, has obvious relevance to photovoltaic applications as well.

3.1 Metal islands on SOI waveguide structures

3.1.1 Photocurrent enhancement in SOI photodetector

In 1996, Stuart and Hall demonstrated an enhancement in photocurrent of a silicon-on-insulator (SOI) photodetector, due to a film of metal islands deposited on the front surface of the device [18].

The structure of the photodetector is shown in fig. 3.1, containing Si substrate, 160 nm thick active Si layer and silicon dioxide (SiO_2) of 190 nm thickess separating the two silicon layers. The active silicon layer acts as a waveguide, supporting three TE and four TM modes at 560 nm wavelength. A spacer layer of lithium fluoride (LiF) and a thin film (approx. 10 nm) of metal were then deposited on top of the device by using vacuum evaporation. The metal film was then annealed under a nitrogen flow at temperature of 300 °C to form metal islands. Three different metals were investigated: silver, gold and copper.

The transmission spectra were measured for different metal island films by depositing the films on a substrate consisting of 30 nm LiF layer on top of a glass slide. The result is presented in fig. 3.2(a). The photocurrent enhancement G
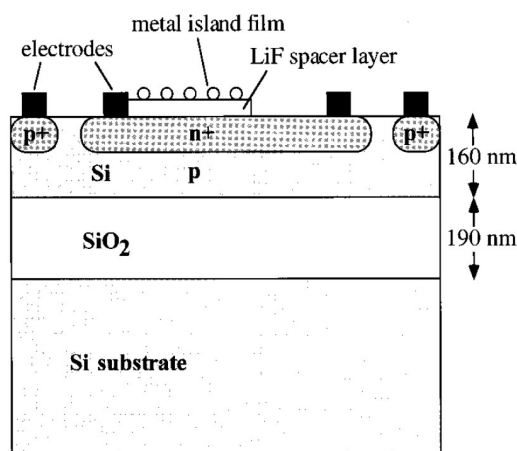
Figure 3.1: Schematic picture of the SOI photodetector used in the measurements, showing the metal island film and spacer layer on front surface [18].

(defined as the ratio of detector photocurrent with metal islands to photocurrent of bare device) in the presence of different metal island films was measured for monochromatic light at normal incidence, and the results are shown in fig. 3.2(b).

Fig. 3.2(b) shows a strong enhancement peak centered around approx. 800 nm wavelength for all three metal island films, the largest and widest peak corresponding to copper with $G \sim 12$. By comparing figs. 3.2(b) and 3.2(a) one can see that the enhancement peak increases in magnitude as the wavelength of bare island resonance (dip in the transmittance curve in fig. 3.2(a)) increases, i.e., as we move from silver to gold to copper. It is also worth noting that for all three metals the enhancement is larger than unity, over almost whole wavelength range shown in the plot. However, there are regions in the short wavelength end of the spectrum in which the photocurrent is decreased due to the presence of the metal island films.

Stuart and Hall conclude that the observed enhancement is almost certainly due to coupling of the metal island resonances to the waveguide modes of the SOI device, based on the fact that the photocurrent enhancement peak increases as the wavelength of the bare island resonance approaches the photocurrent enhancement peak. The optical absorption of Si is stronger at short wavelengths than long – absorptance is 10% at 550 nm whereas it is only 1% at 800 nm – so it is expected that the increase in the photocurrent gives largest relative enhancement at longer wavelengths. Alternative explanations to the enhancement considered by Stuart and Hall are that the island film behaves
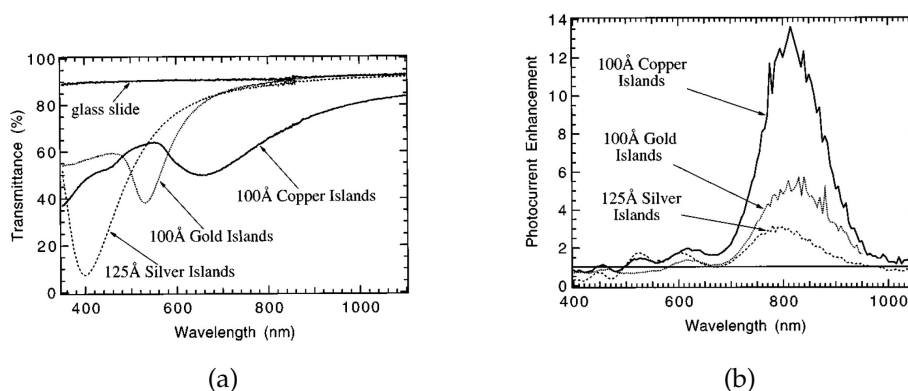
Figure 3.2: (a) Transmission spectra of bare metal island films on a substrate consisting of glass and 30 nm thickness of LiF [18], and (b) photocurrent enhancement in SOI photodetector due to added metal films on top of a 30 nm LiF layer [18]. Dip at the transmittance curve (a) corresponds to the bare island resonance.

as a random scattering layer or an anti reflection coating, but these were ruled out.

3.1.2 Investigation of dipole-dipole interactions in SOI waveguide structures

Continuing their previous studies on metal islands on SOI structures (see previous chapter), in 1998 Stuart and Hall investigated the effect of a nearby waveguide on resonance structure of metal island arrays [19]. For this purpose, a SOI photodetector was used as a test subject. Active Si layer, sandwiched between layers of SiO_2 and LiF, acted as a waveguide. The SOI photodetector used in measurements was similar in construction to that described in chapter 3.1.1. Thickness of the active Si is 160 nm and SiO_2 200 nm. A 30 nm thick layer of LiF and a silver island film of thickness corresponding to an average particle diameter of $\sim$100 nm were fabricated on top of the device as in chapter 3.1.1. The device structure is depicted in the inset of fig. 3.3(a).

The transmission spectrum of bare Ag-island film on top of a 30 nm LiF layer on glass substrate was measured, as well as photocurrent enhancement in the SOI photodetector coated with a similar Ag-island layer. The results of these measurements are shown in fig. 3.3(a), and are quite similar to figs. 3.2(a) and 3.2(b). The dip in the transmission corresponds to a peak in extinction and shows the LSP resonance of Ag islands on LiF and glass at $\lambda \sim 430$ nm. Because for particles of 100 nm diameter scattering dominates over absorption
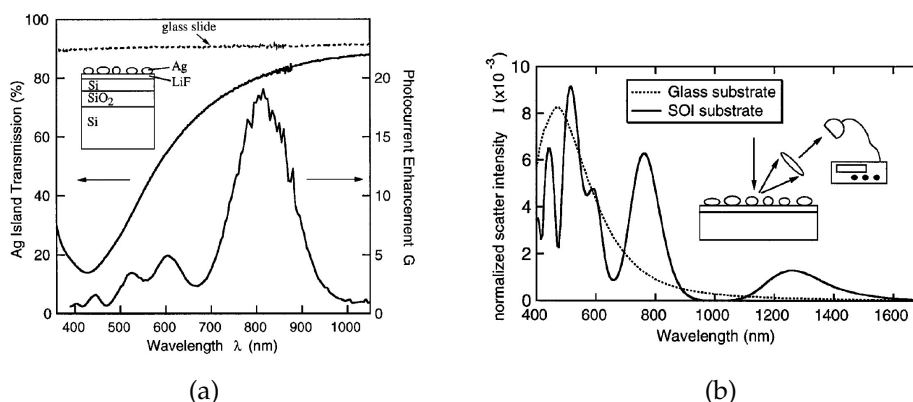
Figure 3.3: (a) The transmission spectrum of a Ag-island film on a LiF-coated glass substrate and measured photocurrent enhancement in a SOI photodetector coated with a similar Ag-island film [19]. (b) Intensity of light scattered from a Ag-island film on a LiF-coated glass substrate and on a SOI photodetector [19].

in the extinction (see fig. 4.1 in chapter 4), the dip in transmission also represents a peak in scattering. The measured photocurrent enhancement shows a large peak near $\lambda = 800$ nm with $G \sim 20$ and several smaller peaks. It can be seen that the peak in the photocurrent enhancement does not coincide with the LSP resonance wavelength of Ag islands. Stuart and Hall explain this by interaction of Ag island resonance and SOI waveguide modes, which alters the resonance structure of metal island array. To investigate this, the intensity of light scattered from the array of Ag islands was measured. Results, depicted in fig. 3.3(b) show that the scattering intensity spectrum is indeed very different for the island-waveguide system to that of the Ag islands on the glass substrate. The peaks in the scattering intensity of the island-waveguide system roughly coincide with the peaks in the photocurrent enhancement. The scattering intensity can be interpreted as a measure of polarizability of the coupled island-waveguide system (as scattering cross section of a nanoparticle is directly proportional to its polarizability, see section 2.3.3).

Stuart and Hall report that increasing the thickness of LiF layer – and thus the separation of the Ag islands from the SOI waveguide – does not alter the number of peaks but shifts the wavelengths of the peaks to longer wavelengths (redshift). This is consistent with the assumption that the altered resonance structure is produced by the coupling of nanoparticles and waveguide modes. This assumption is further supported by observation that the peaks get weaker when separation is increased over 170 nm.

In conclusion, Stuart and Hall report a significant change in resonance struc-

ture of Ag island film in the presence of a waveguide. They believe these effects are caused by strong coupling between LSPs on the Ag islands and the propagating modes in the waveguide. In this paper, Stuart and Hall also theorize that the strong photocurrent enhancement observed here is due to increased interaction between the metal nanoparticles, mediated by the waveguide. However, this suggestion is later disapproved by Catchpole and Pillai [20, 21]. They develop a theoretical model, presented in aforementioned references, which suggests that the photocurrent enhancement structure of a coupled metal island-waveguide system is produced by enhanced scattering cross section for waveguided light (see chapter 4 for further details). It is therefore a single particle, rather than waveguide mediated multi particle effect.

3.1.3 Effects of the metal island size on photocurrent enhancement in SOI photodetectors

The effect of metal island size on photocurrent enhancement in nanoparticle-enhanced SOI photodetectors was investigated by Stuart and Hall in 1998 [22]. The construction of the photodetector is, again, similar to that in chapter 3.1.1 (see fig. 3.1). Silver nanoparticles were chosen to be used in the experiments, because of their high radiative efficiency (see fig. 2.11). The silver island films of different thicknesses were fabricated by similar means to those used in chapter 3.1.1, on top of 30 nm LiF spacer layer. Scanning electron microscope (SEM) images of the Ag island films are presented in fig. 3.4. From the SEM images, the island densities can be approximated to be 1.4×10^{10}, 8.5×10^9 and 3.5×10^9 cm^{-2} for 40, 66 and 108 nm average particle diameter, respectively.

Bare island resonance of the metal islands deposited on a substrate consisting of 30 nm LiF over glass was measured for reference, and the results are shown in fig. 3.5(a). According to electrostatic theory of LSPs (see chapter 2.3.3), only
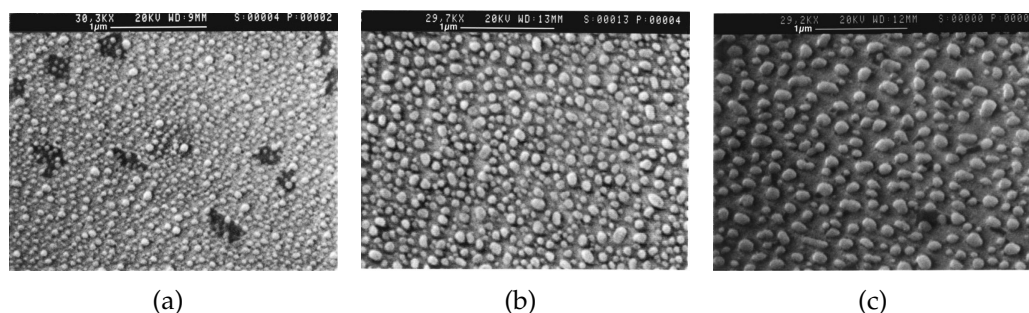

(a)   (b)   (c)

Figure 3.4: SEM images of Ag island films used in the experiments, with average particle diameter of (a)40 nm, (b)66 nm and (c)108 nm [22].
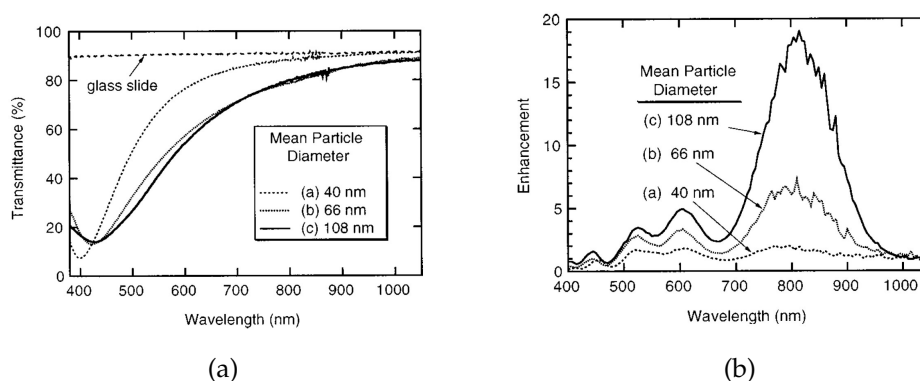
Figure 3.5: Transmission spectra of Ag-island films on a LiF-coated glass substrate (a), and photocurrent enhancement in SOI photodetector due to Ag island films of different thicknesses (b). [22]

the shape, and not the size, of the particles affects the LSP resonance wavelength. The transmission spectra for films (b) and (c) are consistent with theory as they are very similar to each other. However, for some reason, the spectrum for film (a) looks somewhat different from those for (b) and (c).

Photocurrent enhancement G in the SOI detectors was also measured, and the results are shown in fig. 3.5(b). It can be seen that the enhancement increases dramatically as the particle size increases, largest enhancement being $G = 18$ corresponding to particle diameter of 108 nm. However, Stuart and Hall report that further increase in the island size causes a reduction to the enhancement, probably because of two factors: the particle size growing beyond the sub-wavelength scale constraint, and tendency of the manufacturing of larger particles to produce irregular particle shape, which lead to enhanced multipole oscillations and decreased scattering (see chapter 2.3.3).

Stuart and Hall conclude that the observed improvements arise from two physical mechanisms: the increase of the scattering efficiency as the particle size increases, and a qualitative change in the resonance characteristics of the metal island film – i.e. increased polarizability at wavelengths far from the bare island resonance of Ag. The latter is caused by radiative coupling to the waveguide modes of SOI device, as described in chapter 3.1.2. Fig. 3.5(b) suggests that the latter mechanism contributes strongly to the photocurrent enhancement, as the largest enhancement peaks centered around 800 nm wavelength correspond to a maximum in scattering spectrum of the Ag-island/SOI system (see fig. 3.3(b)) at $\lambda \sim 780$ nm.
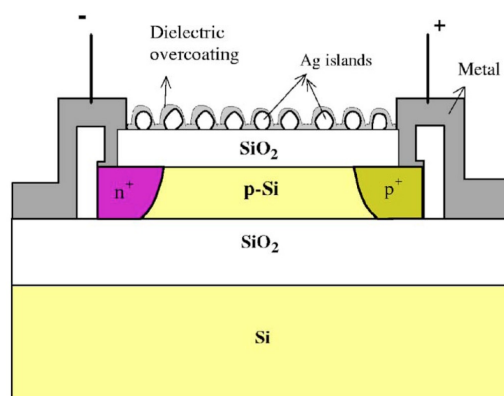
Figure 3.6: A schematic picture of the SOI LED used in the study of effect of Ag nanoparticles on Si LEDs [12].

3.1.4 Enhanced optical emission and absorption in SOI LEDs

In 2006, Pillai *et al.* studied the possibility of exploiting LSPs on Ag nanoparticles to enhance optical emission and absorption of thin Si devices [12]. A silicon-on-insulator (SOI) LED with an active layer of 95 nm thick p-doped silicon was used as a test device (fig. 3.6). To study the effects of the LSP resonance of metallic nanoparticles, a 14 nm thick silver layer was deposited on top of the device, using vacuum evaporation, and then annealed in nitrogen at $200\,°\mathrm{C}$ to form silver islands of around $120 - 140$ nm diameter and $45 - 60$ nm height in average. With surface recombination being the dominant recombination mechanism in SOI devices, a passivating silicon dioxide (SiO_2) layer was placed on top of the active layer. Thickness of this passivating layer was kept to a minimum (35 nm) to ensure a good coupling between the silver islands deposited on top of the SiO_2 layer and the active p-Si. In order to investigate the effect of the Ag nanoparticles on the emission and absorption of the device, electroluminescence (EL) and spectral response (SR) measurements were executed on a plain SOI LED, with Ag islands deposited on top of the device, and finally with Ag islands overcoated with a layer of zinc sulfide (ZnS).

Most interesting measurement in the framework of this thesis, concentrating on the photovoltaic applications of metal nanoparticles, is the SR measurement of the photocurrent enhancement of the SOI device, which can be used as a solar cell as well as a LED. The result of this measurement is presented in fig. 3.7(a). The most significant observation from the figure is that the enhancement is larger than unity for all wavelenghts between approx 500 and 1050 nm, i.e. almost the whole optical spectrum. Addition of the ZnS overcoating produces a redshift of 70 nm to the enhancement peak.
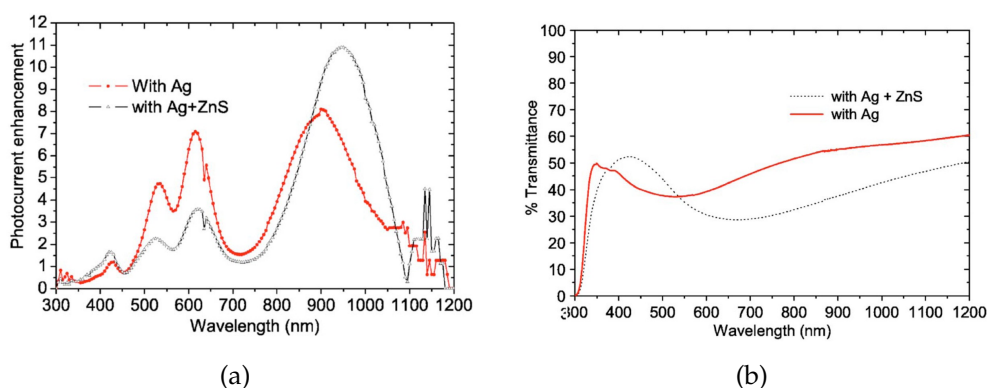
(a) (b)

Figure 3.7: Photocurrent enhancement in the SOI LED with Ag islands and Ag islands overcoated with ZnS (a), and effect of ZnS coating on the bare island resonance (b). [12]

To further study the shift in the LSP resonance caused by the dielectric coating of the Ag particles, a bare island transmittance measurement was carried out for silver islands deposited on top of a glass substrate, with and without the ZnS overcoating. The result is shown on fig. 3.7(b), revealing a redshift in the dip in the transmittance curve i.e. extinction peak (extinction being the complement of transmission).

Pillai *et al.* conclude that the observed enhancements in emission and absorption of the SOI device are due to strong coupling of the LSPs on the Ag particles with the waveguide modes of the active Si layer between the SiO_2 layers. This is claimed to happen when the particles are situated within the near field of the waveguide. From fig. 3.7(b) it can be seen that the extinction – and thus also the scattering – by nanoparticles decreases with increasing wavelength in the case of the bare Ag islands. Pillai *et al.* conclude that if the scattering in the presence of a waveguide is concidered to be a product of the bare island resonance and some factor describing the interaction between the nanoparticles and the waveguide modes, then the redshift in the bare island resonance also produces a shift in the scattering peaks of the whole device. Fig. 3.7(a) shows that the shift is larger at longer wavelenghts, which is reasonable since also the shift in the bare island resonance is larger at longer wavelengths.

In conclusion, Pillai *et al.* report an increase in photocurrent of a SOI device, capable of functioning as a photovoltaic cell as well as a LED, due to surface plasmon excitations on added silver nanoparticles. Also, a redshift in the photocurrent enhancement peak and enhancement in photocurrent is reported upon addition of ZnS overcoating on the silver islands.
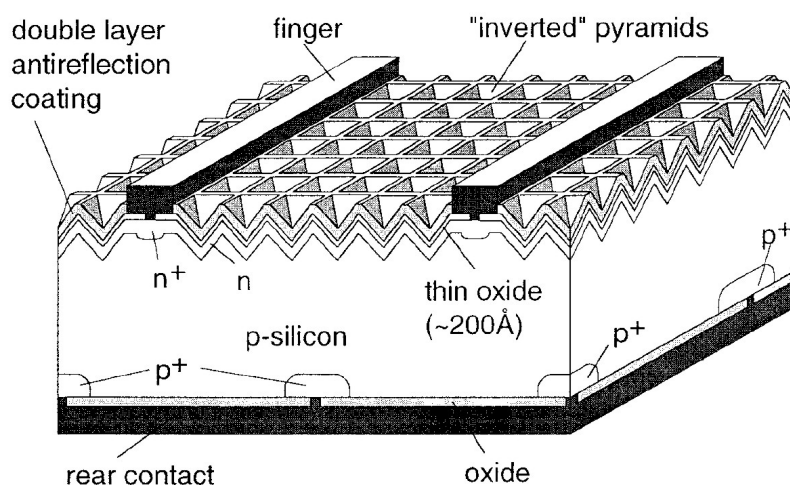
Figure 3.8: Structure of a PERL cell. [23] Thick wafer based Si cell used in the experiments is similar to the cell presented here, with exception that it lacks the inverted pyramid structure. [3]

3.2 Metal islands on SOI and wafer-based Si solar cells

In 2007, extending their previous study of enhanced emission and absorption in SOI LED's due to surface plasmon excitations in silver islands (see section 3.1.4), Pillai *et al.* investigated the enhancement of the photocurrent in silicon solar cells by similar exploitation of LSPs on silver nanoparticles [3]. Devices subject to investigation were SOI-structured thin-film silicon solar cells as well as a thick planar PERL (Passivated Emitter, Rear-Locally diffused) cell made of silicon wafer.

The SOI test cell consisted of 30 nm thick top oxide (SiO_2), 1250 nm layer of active Si, and 1000 nm layer of buried SiO_2 on top of a Si substrate. The wafer-based Si solar cell used in experiments, a 300 μm thick planar PERL type cell with 30 nm top oxide, is presented in fig. 3.8. The silver islands were deposited on top of both devices, again, by thermal evaporation followed by annealing. SEM images of the Ag island films are shown in fig. 3.9, from which the approximate particle densities are 3.5×10^9, 1.0×10^9, 1.0×10^9 and 4.0×10^8 cm^{-2} for 14, 16, 18 and 27 nm mass thickness, respectively.

As usual, the bare island resonance of Ag particles was measured for particles deposited on glass. The transmittance for bare Ag island films of different mass thicknesses are presented in fig. 3.10, showing redshifting of the resonance with increasing mass thickness. This shift in resonance wavelength is due to the particle shape coming more oblate and irregular in the annealing
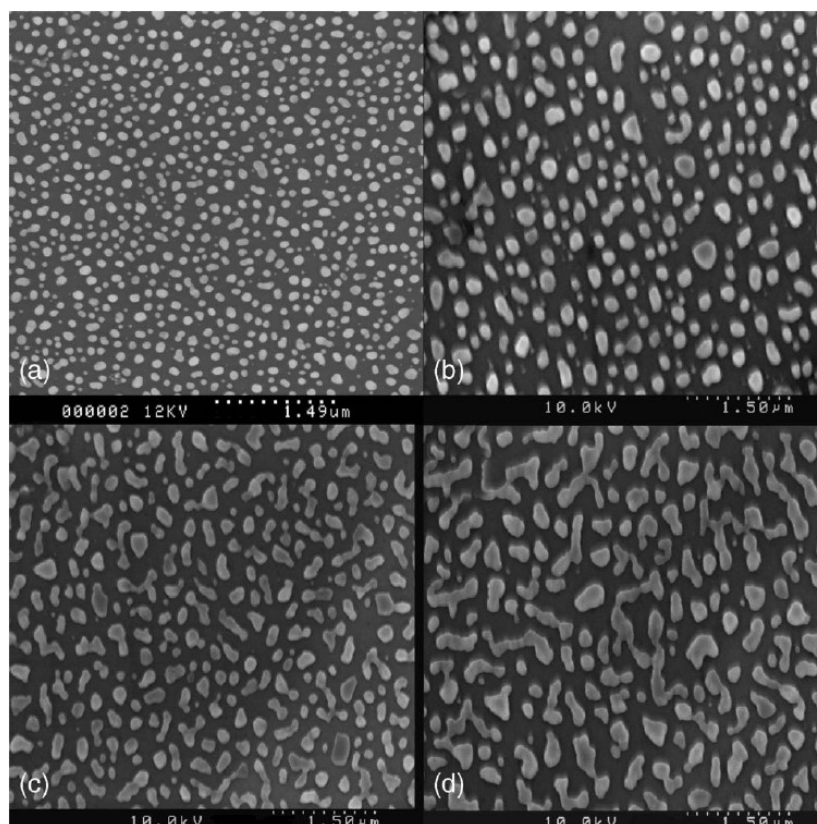
Figure 3.9: SEM images showing the Ag island films of (a) 14 nm, (b) 16 nm, (c) 18 nm, and (d) 27 nm mass thickness. Note the variation in average particle size, from approx. 120 nm for (a), to 350 nm for (d). [3]
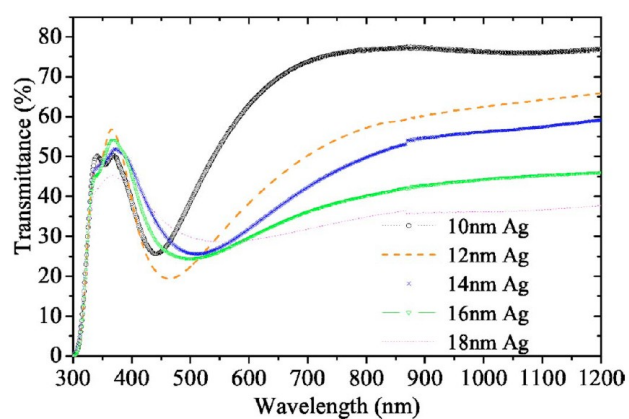

Figure 3.10: Transmittance of bare Ag island films for different mass thicknesses [3].

process, as the particle size increases. The plot also shows broadening of the resonance peak with increasing mass thickness. Pillai *et al.* state that this is probably caused by depolarization effects for larger particles and averaging of the resonance over different particle shapes in the film.

The photocurrent enhancements due to the added silver island films for SOI- and wafer based test cells are shown in figs. 3.11(a) and 3.11(b), respectively. The plots for SOI cell show a maximum enhancement of $G = 16$ for 16 nm mass thickness of silver, with 16% total increase in photocurrent, averaged over the AM1.5 spectrum, and $G = 13$ with 33% total increase for 12 nm mass thickness. The 300 micron thick planar PERL cell shows 3-, 4- and 7-fold maximum enhancements for 12, 14 and 16 nm mass thickness, respectively, corresponding to a total increase of 19%, 14% and 2% for the AM1.5 spectrum. The enhancement factor is larger than unity for all wavelengths above 500 nm.

Further measurements were made with a double-sided polished silicon wafer, with and without Ag island films. Layer dimensions of the silicon wafer were similar to the planar PERL cell. Absorptance and reflectance plots are shown in figs. 3.12(a) and 3.12(b), respectively. It is illustrative to compare the absorptance enhancement spectrum to the photocurrent enhancement spectrum of the wafer based silicon solar cell in fig. 3.11(b). Fig. 3.12(a) shows a large and increasing absorptance enhancement at long wavelengths ($1000 - 1200$ nm) with increasing Ag mass thickness. This can also be observed in the photocurrent enhancement spectrum in fig. 3.11(b). For the smallest 10 nm mass thickness, however, this absorptance enhancement peak is non-existent.

Absorptance enhancement plots also show an additional peak at $\lambda \sim 350$ nm, whereas there's a reduction in photocurrent enhancement. This corresponds to a strong absorption in the Ag islands around this wavelength (see fig. 2.11), which means that energy is absorbed in the silver island film, rather than in the silicon. Comparison of absorptance enhancement and reflectance spectra in figs. 3.12(a) and (b) reveals that the total reflectance is reduced at almost entire wavelength range from visible to near infra-red, whereas the largest absorption enhancement occurs at wavelengths higher than 1000 nm. This means that in the visible region, the Ag island layer acts more like an antireflection coating, and the effect of light trapping dominates in the near infra-red.

In conclusion, the measurements show that for the thin SOI device there is a significant enhancement in the photocurrent over the entire spectrum for wavelengths $\lambda > 600$ nm. The enhancement is larger for larger particle size at longer wavelengths, whereas in shorter wavelengths there is a reduction. It is because of this reduction, that the overall photocurrent enhancement over the AM1.5 spectrum is larger for 12 nm Ag island thickness than for 16 nm.
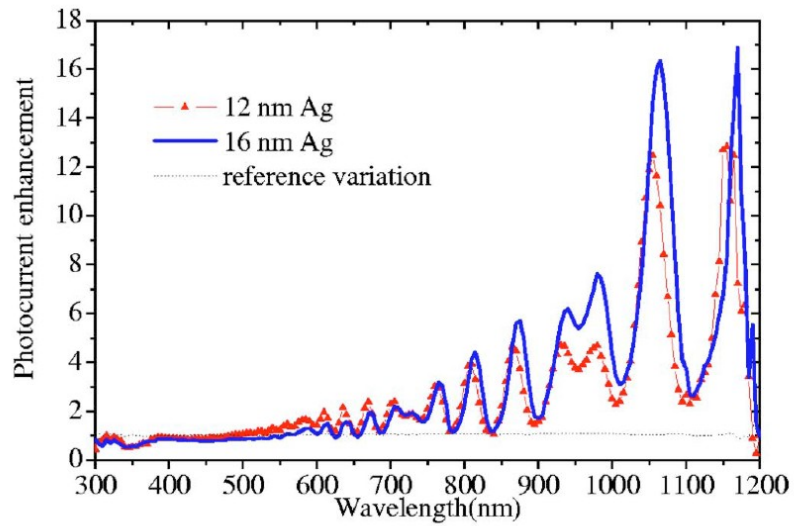
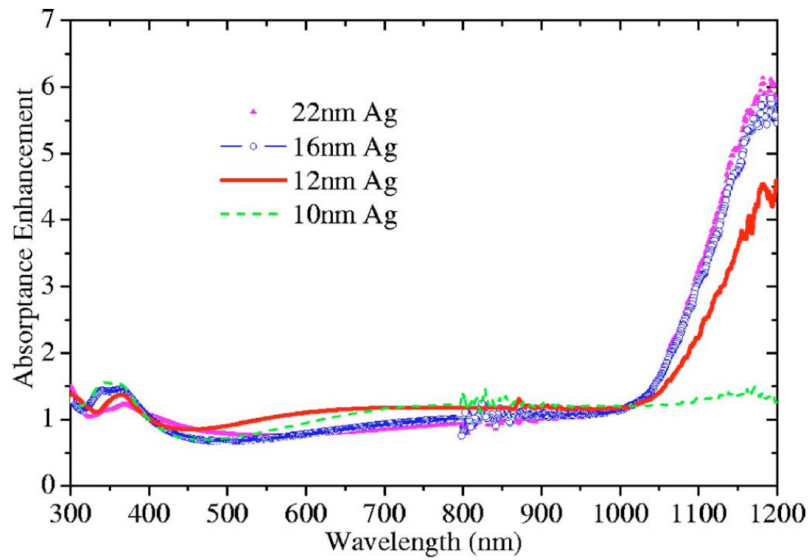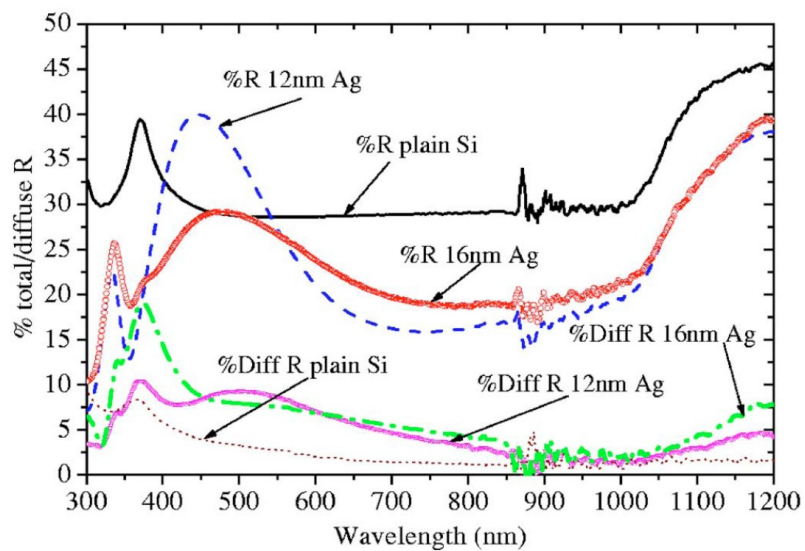(a)
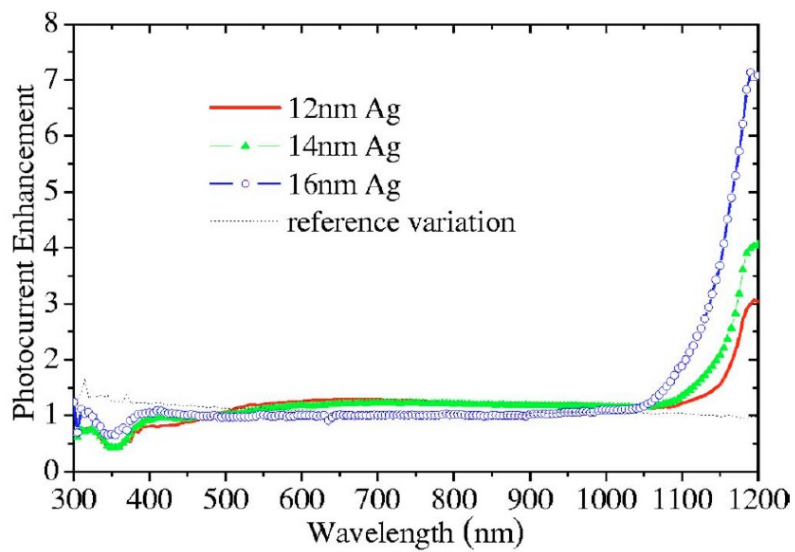
(b)

Figure 3.11: Photocurrent enhancement in a SOI- (a) and a wafer-based (b) solar cell, due to the added Ag islands [3].

(a)

(b)

Figure 3.12: Absorptance enhancement in double-sided polished Si wafer due to added Ag island films (a), and total and diffuse reflectance of double-sided polished Si wafer with 30 nm top oxide (SiO$_2$), with and without Ag island films (b). [3]

For thick wafer-based test cell, there is a significant increase only at the longer wavelengths ($\lambda > 1000$ nm), near the Si band-gap, which is due to the fact that thick Si cell already absorbs efficiently at shorter wavelengths.

Pillai *et al.* conclude that the effect of the increasing particle size is an increase in the radiative efficiency (see fig. 2.11) and the scattering cross section (see fig. 2.8). This effect is more evident for the thick wafer-based Si cells than for the thin-film SOI devices, as can be seen from figs. 3.11(b) and 3.11(a). However, increasing particle size beyond certain limit enables multipole oscillations in the metal particles, decreasing the scattering efficiency. Thus, there is an optimum size for the particles, in order to achieve the best possible enhancement over as broad spectral range as possible.

3.3 Nanoparticles on thin-film Si semiconductors

3.3.1 Enhanced optical absorption in Si semiconductor

In 2005 Schaadt *et al.* reported an enhancement of photoabsorption and photocurrent in a silicon semiconductor, achieved by exploiting LSP resonance in gold nanoparticles on the silicon surface [24]. A schematic picture of the semiconductor device used in the experiments is presented in fig. 3.13. The *pn* junction was fabricated from *n*-type silicon by doping the top part of the wafer *p*-type with boron. Junction depth was calculated to be 80 nm. Ohmic contacts were made of aluminum, with thickness of approx. 150 nm. Gold nanoparticles were deposited on the front surface (*p*-side) of the device in colloidal solution. SEM images of the deposited Au particles, with diameters of 50, 80 and 100 nm are shown in fig. 3.14. Corresponding particle densities were approx. 6.6×10^8, 1.6×10^8 and 6.6×10^7 cm^{-2}, respectively. As can be seen from the SEM images, the nanoparticles are present as single particles, rather than in multi-particle clusters. This is a major difference compared to the metal island structures used in the studies in chapter 3.1.

The extinction spectra of the Au nanoparticles were measured by placing the particles in aqueous solution in a rectangular glass cell. The extinction efficiency was defined as $\log(T_C/T_{Au})$, where T_C is the intensity of light transmitted through a glass cell containing only de-ionized water, and T_{Au} the intensity of light transmitted through a glass cell containing the Au particle solution. A graph of the measured extinction efficiencies, as defined above, is presented in fig. 3.15. It shows clear peaks corresponding to plasmon resonances. It can be observed, that the resonances broaden and exhibit a redshift as the particle size increases.
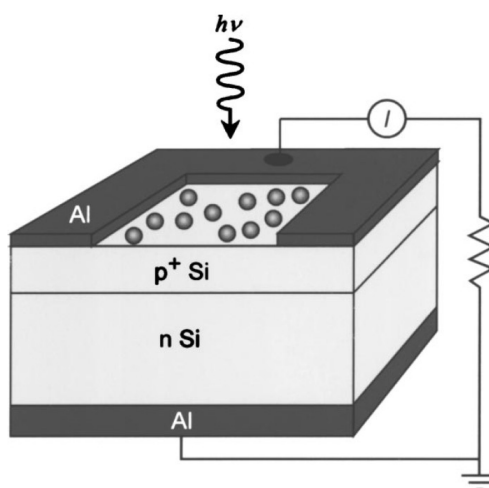
Figure 3.13: Schematic picture of the Si semiconductor device used in the experiments, with illumination and measurement set up. Note the Au nanoparticles on the front surface (p-side). [24]

(a)   (b)   (c)
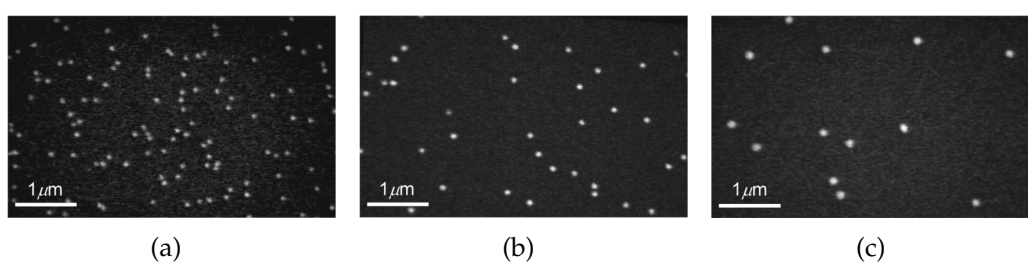
Figure 3.14: SEM images of Au nanoparticles deposited on the Si *pn* junction diode surfaces, with particle diameters of (a) 50 nm, (b) 80 nm, and (c) 100 nm [24]. Particle densities are approx. 6.6×10^8, 1.6×10^8 and 7.7×10^7 cm^{-2}, respectively. Note the difference in particle spacing to metal island structures in figs. 3.4 and 3.9.
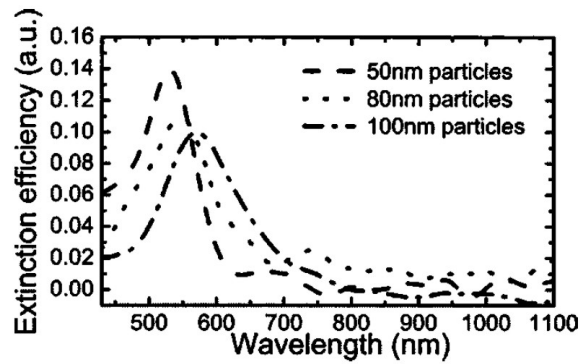
Figure 3.15: Extinction efficiency of Au nanoparticles of different diameters suspended in aqueous solution [24].

(a)   (b)
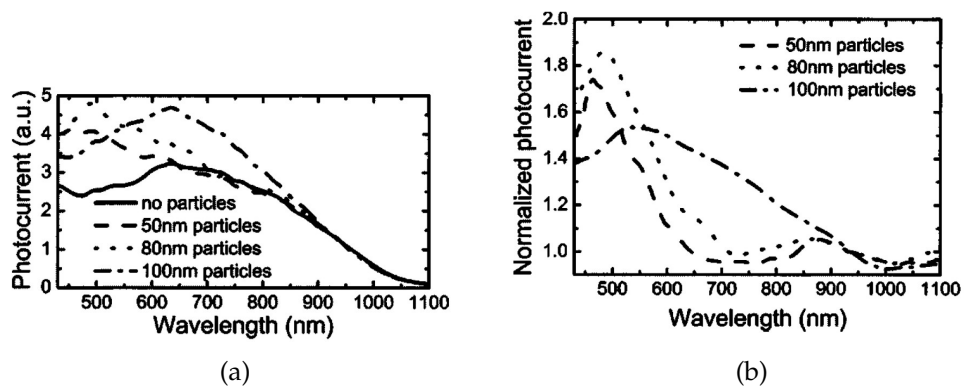
Figure 3.16: Photocurrent of Si *pn* junction diode with and without Au nanoparticles (a), and photocurrent normalized to Si diode without nanoparticles (b). [24]

The photocurrent response of the Si *pn* junction diode was measured for devices with and without Au nanoparticles. Results are shown in fig. 3.16, with fig. 3.16(a) showing the absolute photocurrent and fig. 3.16(b) the normalized photocurrent, in respect to the photocurrent without Au particles. All the spectra have been normalized to account for the source illumination spectrum, and scaled so that the photocurrent response is similar for wavelengths of $950 - 1100$ nm, in order to remove variations due to external factors of the measurements. Schaadt *et al.* presume, that in this wavelength area the added Au nanoparticles do not contribute significantly into the photocurrent, based on the extinction spectra in fig. 3.15. However, in the light of extinction and photocurrent enhancement spectra presented in the studies in chapter 3.1, this seems a bold assumption. Comparison of, for example, figs. 3.10 and 3.11 implies that the metal particles can also affect the photocurrent response of the Si semiconductor at the wavelengths far away from the bare metal particle resonance.

From figs. 3.16(a) and 3.16(b), a considerable photocurrent enhancement over a wide wavelength range can be observed for all Au particle sizes. The maximum peak enhancement of factor ~ 1.8 is observed for 80 nm particle diameter, but particle diameter of 100 nm produces the widest enhancement peak, extending from $\lambda \sim 900$ nm downwards, with maximum enhancement factor of roughly 1.5. For particle diameter of 50 nm, the enhancement factor drops below unity – meaning a decrease in photocurrent – at wavelengths of approx. 650 to 800 nm. All particle sizes show a decrease in photocurrent at wavelengths above ~ 950 nm. The enhancement peak shifts towards longer wavelengths as the particle size increases. All in all, the photocurrent enhancement response observed here differs greatly from those obtained in chapter 3.1, with metal island films.

Schaadt *et al.* credit the observed photocurrent enhancement to increased optical absorption in Si, due to the surface plasmon excitations in the Au nanoparticles. Two primary reasons for this are considered: First, the amplitude of electric field near a metal nanoparticle, due to the LSP excitation, is significantly larger than the amplitude of the incident field, giving rise to enhanced optical absorption in semiconductor region in close proximity to the particles. Second, the duration of the interaction between the incident electromagnetic field and the semiconductor is increased near the metal particles, as the life-time of an LSP excitation is some $\sim 5 - 10$ times greater than the photon transit time through the distance of the LSP near field (~ 100 nm).

Apart from the LSP excitations, an alternate explanation for the observed photocurrent enhancement could, according to Schaadt *et al.*, be generation of

charge carriers inside the metal nanoparticles, which are then injected into the semiconductor. This carrier generation could occur either directly via photoexcitation in the metal particle, or via plasmon decay, which generates an electron-hole pair. However, the direct carrier generation in the metal nanoparticles is ruled out by the observation that the photocurrent enhancements occur only at wavelengths corresponding to the LSP resonances. The plasmon decay is eliminated as a possibility, due to the fact that no charging of the nanoparticles was observed; if electron-hole pairs were generated in the particles and electrons then injected to semiconductor, the metal particles would accumulate positive charge.

Schaadt *et al.* conclude that, considering the short diffusion lengths of the charge carriers in the Si *pn* diode, a photocurrent enhancement is expected if the carrier generation is increased specifically near the junction region of the device. It is also stated that increased carrier generation should not be confined to region near the silicon diode surface, where the surface recombination is significant. In short, Schaadt *et. al* demonstrate an enhancement in photocurrent of a Si *pn* junction diode, due to LSP excitations in Au nanoparticles, and their proposition of the mechanisms responsible for this enhancement is quite different to those presented in chapter 3.1.

3.3.2 Gold nanoparticles in *a*-Si solar cells

Derkacs *et al.* investigated the enhancement of *a*-Si:H solar cell's performance by LSP excitations in Au nanoparticles in 2006 [25], and reported an 8.1% enhancement in short-circuit current and an 8.3% enhancement in energy conversion efficiency.

The 240 nm thick amorphous silicon *p-i-n* test device, shown in fig. 3.17(a), was fabricated on a stainless steel substrate by chemical vapor deposition. Indium tin oxide (ITO) contacts, 20 nm thick and 500 μm in diameter, were deposited by sputtering, on contact patterns formed on the *p*-type surface by optical lithography. The Au nanoparticles were deposited in a colloidal solution, like in chapter 3.3.1. The particle diameter was 100 nm and density 3.7×10^8 cm^{-2}, as shown in a SEM image in fig. 3.17(b).

The test cells were illuminated at normal incidence with a quartz-halogen bulb through a monochromator, and current density versus cell voltage was measured. The resulting *J-V* and *P-V* curves are presented in fig. 3.18. The current density and the power output curves are drawn from averages across all eight test devices. The measurements with the Au nanoparticles show an increase from 6.66 to 7.20 mA/cm^2 in the short circuit (V=0) current density, corresponding to 8.1% relative increase, and an 8.3% increase in the total

(a)   (b)

Figure 3.17: (a) Schematic figure of the a-Si:H p-i-n test cell used in the experiments [25]. (b) SEM image of the Au nanoparticles deposited on the device surface [25]. Particle diameter is 100 nm and density 3.7×10^8 cm^{-2}.
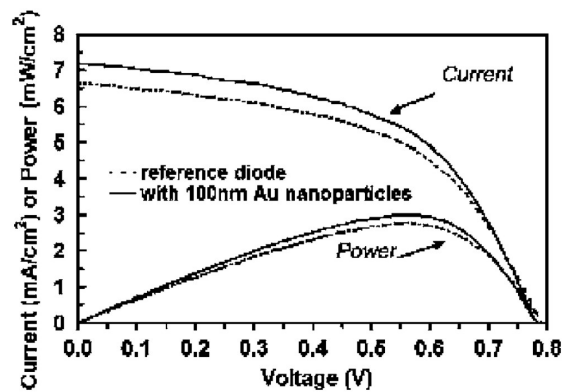
Figure 3.18: *J-V* and *P-V* characteristics of the *a*-Si:H *p-i-n* test cells without Au nanoparticles (dashed lines), and of the same cells after deposition of the nanoparticles (solid lines). [25]
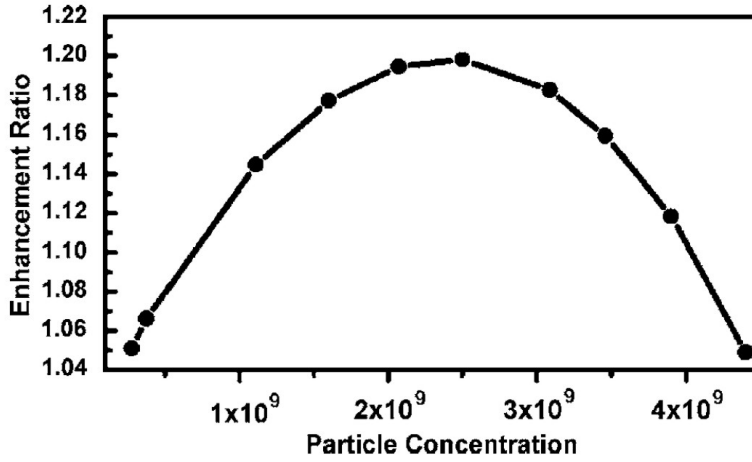
Figure 3.19: Enhancement ratio R_p, defined as ratio of $|E_0|^2$ integrated over a-Si:H layer for cell with Au particles to that of a cell without nanoparticles, simulated for incident radiation with $\lambda = 600$ nm. Particle concentration is given in cm^{-2}. [25]

power output – and consequently, in energy conversion efficiency – from 2.77 to 3.00 mW/cm^2.

Derkacs *et al.* explain the observed enhancements with combination of Mie theory for isolated particles, and computational electromagnetic simulations, taking into account the particle-particle, particle-substrate and particle-substrate-particle interactions. The simulations of the test cells showed enhanced electromagnetic field amplitude in the *a*-Si:H layer below the nanoparticle, caused by the strong forward scattering of the incident wave from the nanoparticle. To investigate the effect of nanoparticle density to the device performance, the square of the electric field amplitude $|E_0|^2$ integrated over the entire *a*-Si:H was taken as a measure of the optical absorption in the simulated solar cell. Then, enhancement ratio R_p was defined as the ratio of $\int_V |E_0|^2$ of a cell with added nanoparticles to that of a device without particles. fig. 3.19 shows plot of R_p, obtained from the electromagnetic simulations for incident radiation at $\lambda = 600$ nm, for different particle densities. Simulation produces maximal enhancement at around particle density of 2.5×10^9 cm^{-2}, as opposed to 3.7×10^8 cm^{-2} used in the measurements, which indicates that efficiency enhancements much larger than observed here could be achieved with higher particle consentrations. The ratio R_p at the optimal particle consentration is approximately three times higher than near the particle density used in the experiments here. However, note that the $\int_V |E_0|^2$ is only an approximate measure of the photogenerated current in a semiconductor.
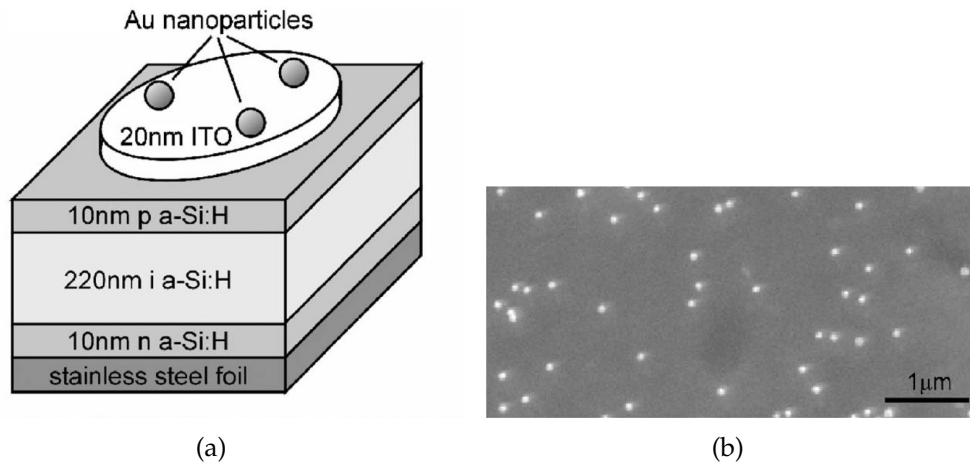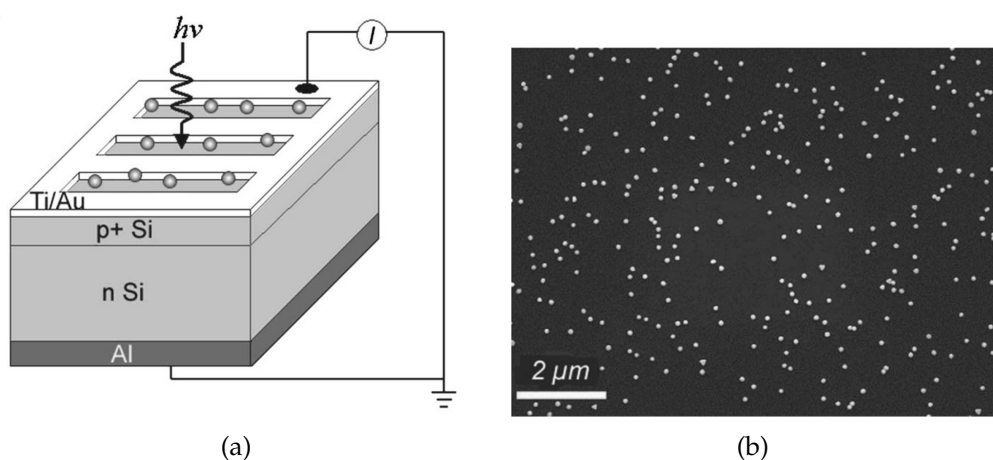
(a)   (b)

Figure 3.20: (a) Schematic figure of the Si *pn* photodiode used in the experiments [8]. (b) SEM image of the Au nanoparticles deposited on the device surface [8]. Particle diameter is 100 nm and density approx. 3.5×10^8 cm^{-2}.

3.3.3 Optical absorption in Si semiconductor: further analysis

Effect of gold nanoparticles on photoabsorption in Si *pn* junction diode was further investigated by Lim *et al.* in 2007 [8]. Photocurrent enhancement was observed at wavelengths above LSP resonance wavelength of Au nanoparticles, but presence of the nanoparticles also produced a noticeable decrease in the photocurrent at wavelengths below the LSP resonance. Lim *et al.* also employed the Mie theory and simulations to explain the observed behaviour.

The structure of the test photodiodes, manufactured by diffusing boron into *n*-type Si wafer, with estimated junction depht of 0.5 μm, is very similar to the Si *pn* junction diode used in chapter 3.3.1. A schematic picture of the device is shown in fig. 3.20 together with a SEM image of the Au nanoparticles deposited on the device in colloidal solution. Front contacts were made of 20 nm titanium and 80 nm gold, and the back contact of 200 nm aluminum. Au nanoparticle diameter was 100 nm with particle density of $\sim 3.5 \times 10^8$ cm^{-2}.

Photocurrent measurements were performed with illumination from a tungsten-halogen lamp through a monochromator, for devices with nanoparticles and reference diodes with no particles. Photoresponse of the reference device is presented in fig. 3.21(a), showing a typical Si diode photocurrent spectrum. Fig. 3.21(b) shows the photocurrent enhancement of the device with added Au nanoparticles. Enhancement peak is observed at approx. 680 nm, which corresponds to the 100 nm diameter Au particle resonance, taking into account the dielectric environment (poly-L-lysine solution used to immobilize

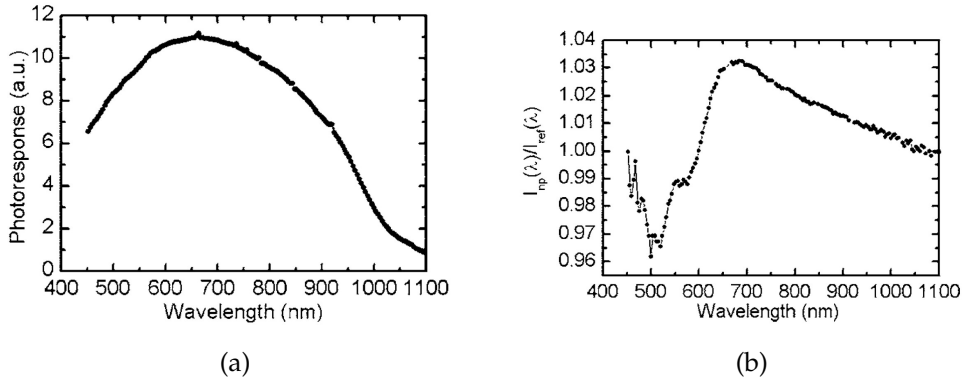(a)   (b)

Figure 3.21: (a) Photocurrent of the reference Si *pn* photodiode [8]. (b) Photocurrent enhancement in Si *pn* photodiode with the added Au nanoparticles, taken as the ratio of photocurrent in device with added nanoparticles to photocurrent of the reference device [8].

the nanoparticles on the device surface), and the enhancement extends all the way up to $\lambda = 1100$ nm. The magnitude of the enhancement, however, is considerably more modest than those obtained in the previous studies, peaking at approx. factor 1.03. The most notable behaviour observed here is the decrease in photocurrent at wavelengths shorter than the resonance wavelength, magnitude of the decrease being comparable to the increase at longer wavelengths. Lim *et al.* credit the observed increase at $580 - 1100$ nm wavelengths to strong forward scattering from the Au nanoparticles.

Numerical simulations were employed in order to investigate the mechanisms behind the observed behaviour. Fig. 3.22 shows the simulated electric field magnitude for an electromagnetic plane wave incident on a Si semiconductor device. It can be seen that single Au nanoparticle above the device surface produces enhanced electric field magnitude inside the semiconductor region, due to the strong forward scattering by the particle. Enhanced electric field magnitude is observed to the immediate right from the particle, and decreased field magnitude to the immediate left. Interactions between particles were taken into account. The squared electric field amplitude integrated over the Si semiconductor volume $G = \int |\mathbf{E}|^2$ was taken as a measure of the optical absorption in the semiconductor device. Fig. 3.23 shows G of a Si semiconductor with added Au nanoparticles normalized to a reference device without nanoparticles, showing apparent resemblance to the experimentally measured photocurrent enhancement in fig. 3.21. This leads Lim *et al.* to a conclusion, that the decrease in photocurrent at wavelengths below the LSP resonance is due to decreased electric field amplitude. They further explain that the reduc-
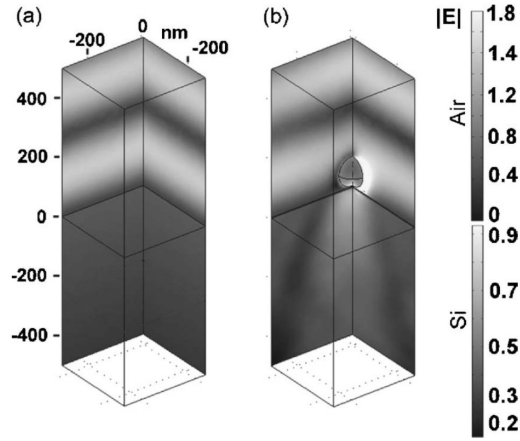
Figure 3.22: Simulated electric field magnitude for an electromagnetic plane wave with 550 nm wavelength incident on (a) Si semiconductor and (b) Si semiconductor with single 100 nm Au nanoparticle 2 nm above the Si surface. [8]
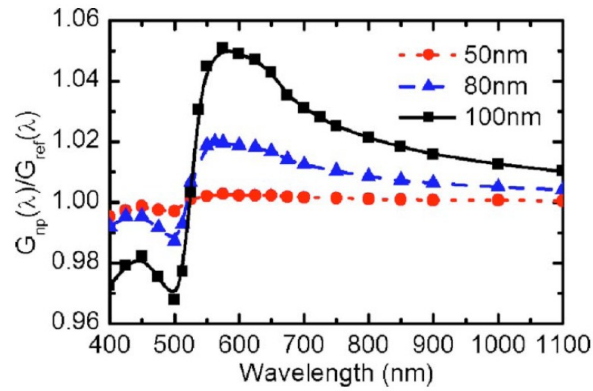
Figure 3.23: Simulated squared electric field amplitude $|\mathbf{E}|^2$ integrated over the Si semiconductor volume for an electromagnetic plane waves incident on the Si semiconductor device with Au nanoparticles of 50, 80 and 100 nm diameter. Normalized to reference device without added nanoparticles. [8]
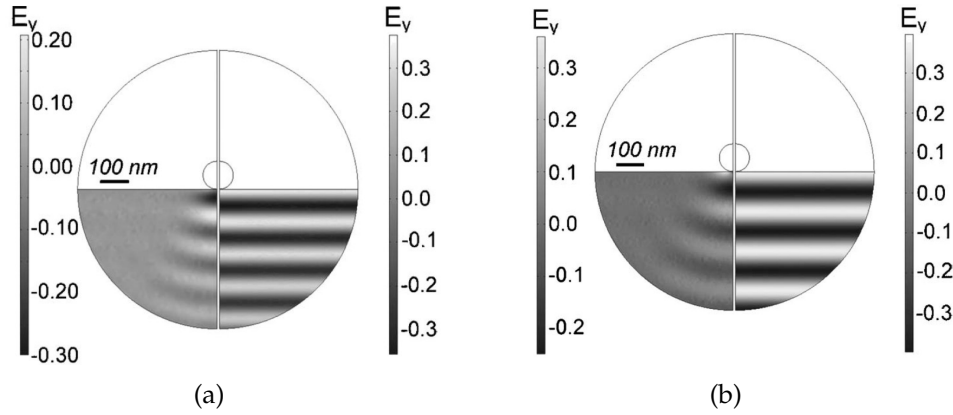
Figure 3.24: Simulated y component of the electric field in the Si semiconductor in the presence of a spherical Au nanoparticle of 100 nm diameter for incident electromagnetic radiation at (a) 500, and (b) 575 nm wavelength. Bottom half of the circle represents the semiconductor region, lower left quadrant showing the scattered, and lower right quadrant the transmitted electric field. Electromagnetic radiation is propagating at z direction (vertical axis in the figure). Note the phase difference between the transmitted and the scattered waves in (a). [8].

tion or increase in the electric field amplitude arises from interference between the transmitted part of the incident electromagnetic radiation and the wave scattered by the Au particles.

As seen in chapter 2.3.3, a subwavelength sized spherical particle in an incident oscillating electric field can be approximated as a point dipole, polarization of which is given by $\mathbf{p} = \alpha \mathbf{E}_0$. Oscillating dipole scatters the incident electromagnetic radiation, and the scattered field is directly proportional to the polarization $\mathbf{p}$, which in turn is proportional to the wavelength dependent, complex polarizability $\alpha = |\alpha|e^{i\gamma}$, given by equation (2.26). The phase angle γ is then the phase difference between the exciting field and the electric field of the oscillating dipole, and determines whether the interference is of constructive or destructive nature. As seen in chapter 2.3.3, there is a large phase shift in α at wavelengths near the LSP resonance wavelength, meaning phase difference between the transmitted and scattered fields and thus destructive interference. This effect is illustrated by fig. 3.24, which presents simulated electric field of the electromagnetic radiation in silicon for radiation propagating at z direction. Note that total electric field is obtained by adding the transmitted and scattered fields.

Lim *et al.* conclude that the nanoparticles differ from antireflection coating of solar cell in that the electric field enhancement due to an AR coating is

uniform throughout the entire semiconductor volume, whereas the nanoparticles produce high local field intensities immediately underneath the particles. The nanoparticles can produce photocurrent enhancement over broad spectral range, but also a reduction at wavelengths below the LSP resonance wavelength. Thus, for solar cell applications, it is important to tune the range of the photocurrent reduction away from the area of interest in incident radiation spectrum.

Chapter 4

Discussion

4.1 Coupling LSPs into waveguides

Experiments with metal island films on SOI waveguide structures show high photocurrent enhancement peaks at wavelengths far away from the surface plasmon resonance. This arises from the ability of metal islands to efficiently couple light into the underlying waveguide [18, 19, 20, 21]. Stuart and Hall have proposed that this arises from increased dipole-dipole interactions between the metal islands mediated by the waveguide [19]. Catchpole and Pillai however disapprove this interpretation. Their theoretical model suggests that the scattering cross sections of individual metal particles are enhanced strongly by the interaction with a waveguide, and this gives rise to the observed photocurrent enhancement spectra [20, 21]. This would mean that the enhancement is a single particle effect, rather than a multiparticle effect of interacting dipoles. Catchpole and Pillai describe the process as follows [20, 21]: Incident electromagnetic radiation excites dipolar plasmon resonances on the metal particles, which then reradiate into multiple directions. Because of the very high refractive index of silicon, vast majority of this radiation is emitted into the SOI device, and trapped into the guided modes of the waveguide. Radiation in these guided modes can then couple back to the plasmon modes in a reverse process. Now, due to the thinness of the active silicon layer, only a few waveguide modes exist, and by the principle of reciprocity of light, the scattering cross section for this light must be very high. Thus, vast majority of the light coupled back to the metal islands is reradiated into the trapped modes in the waveguide. Effectively, incident light at these resonant wavelengths is trapped into modes that propagate in all directions parallel to the waveguide surface [18]. This leads to enhanced optical absorption within the semiconductor.

This can be interpreted from fig. 3.3, where the photocurrent of the SOI photodetector is increased at wavelengths corresponding to diffuse scattering intensity maxima of the coupled semiconductor-metal island system. (Here term "diffuse scattering" is used for scattering out of the SOI device, to differentiate it from the scattering by particles into the waveguide.) Diffuse scattering intensity can be interpreted as a measure of polarizability of the coupled SOI-metal island system [19], as the polarizability of a particle is directly related to it's scattering cross section. Some fraction of the electromagnetic radiation in the guided modes that is coupled back to the metal islands is reradiated out of the waveguide [18, 20], and this shows in the diffuse scattering intensity spectrum. Thus, the diffuse scattering intensity maxima correspond to the wavelengths that are strongly coupled to the trapped waveguide modes.

Maximum increase of 33% in total photocurrent integrated over the AM1.5 solar spectrum is achieved with this silicon-on-insulator geometry, in test cell with Ag island film in ref. [3]. However, specifics of the test cell performance without the added nanoparticles is not available.

4.1.1 Electromagnetic interpretation

In terms of electromagnetics, the phenomenon discussed above could be interpreted as follows: The metal nanoparticles can be in this wavelength regime well approximated as oscillating dipoles, which have electric fields with both non-propagating and radiative parts (see section 2.3.3). Although the non-propagating near field dominates at the limit of r approaching zero, also the radiative part of the field is present at close proximity to the particle. The radiative field is a spherical wave, proportional to e^{ikr}/r, and is spatially distributed into all directions. However, due to the high refractive index of silicon, for nanoparticles deposited on top of a Si waveguide, most of the radiation is directed into the silicon. Catchpole and Pillai [20, 21] describe this as angular dependent scattering cross section of the metal islands caused by interaction with the waveguide. In order to have the radiative modes of the metal nanoparticles to excite electromagnetic modes in the waveguide, conservation of energy and momentum must be obeyed. This sets two conditions for the excitation of a waveguide mode: First, the energy of the plasmon must be higher than or equal to the energy of the waveguide mode. This means that only wavelengths above the plasmon resonance wavelengths can be coupled into the waveguide. And second, only radiation with component of wave vector **k** parallel to the waveguide can be coupled into the waveguide. This means that light at certain suitable wavelengths above bare island resonance wavelength is effectively coupled into the waveguide modes. This is observed as an

increased scattering cross section of the metal islands for these certain wavelengths of light [20, 21]. The coupling efficiency of the dipolar excitation on metal nanoparticle to the trapped modes in SOI waveguide has been shown to be strikingly large ($< 80\%$) [26].

4.1.2 Effect of particle resonance wavelength

The photocurrent enhancement spectra presented in figs. 3.2 and 3.5 are produced by interaction of surface plasmon resonances of metal islands with guided modes of the SOI waveguide. Radiation in guided modes is coupled back to the waveguide by the metal particles multiple times, which leads to a strongly enhanced absorption at the wavelengths of the guided modes supported by the waveguide. Effectively, we observe a number of resonance peaks for the coupled metal island–waveguide system. The position of the photocurrent enhancement peaks is determined by the wavelength of the trapped modes supported by the waveguide. Examination of fig. 3.2 supports this conclusion; each of the three metals under examination – silver, gold and copper – have different resonance wavelengths, but the positions of peaks in photocurrent enhancement is not affected, at least noticeably. This is also true for altering the particle size. There is, however, change in the magnitude of the photocurrent enhancement in both cases. Stuart and Hall presume that the increase in magnitude in case of different metals is due to the bare metal island resonance wavelength approaching the wavelength of strong resonance in the island-waveguide system [18, 22]. Examination of fig. 3.2(a), in which transmission spectra of silver, gold and copper island films used in experiments by Stuart and Hall are presented, supports this assumption; copper has the weakest extinction peak of the three metals under examination, but it is situated nearest to the resonance of the coupled metal island-waveguide system, and produces the highest enhancement.

4.1.3 Effect of particle size

Increasing particle size produces increase in the magnitude of photocurrent enhancement, even if the change in particle size does not considerably alter the LSP resonance wavelength, as seen in fig. 3.5. Intuitively, this could be explained with increasing radiative efficiency and scattering cross section, as particle size becomes larger. Using data of dielectric functions from ref. [17] and eq. (2.35), scattering cross sections of silver sphere at $\lambda = 820$ nm are 2.21, 44.6 and 858 nm^2 for particle diameter of 40, 66 and 108 nm, respectively. However, transmission spectrum of the metal island film in fig. 3.5(a) is not considerably
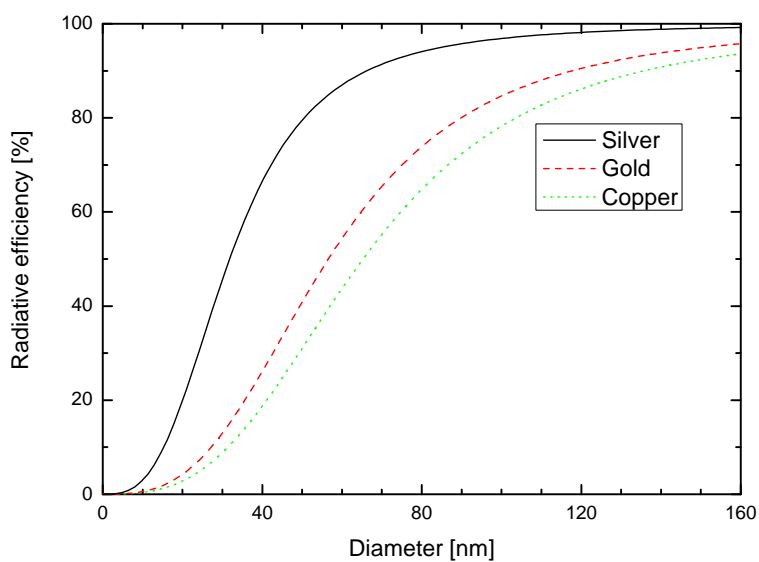
Figure 4.1: Radiative efficiency of a spherical particle, made of silver, gold and copper, as a function of diameter at $\lambda = 820$. Data of dielectric functions taken from ref. [17] and expressions for scattering and absorpion cross sections from eqs. 2.35 and 2.36.

affected by the change in the particle size. Corresponding radiative efficiencies are 0.665, 0.899 and 0.975. This is illustrated in fig. 4.1, where radiative efficiencies of silver, gold and copper, defined as $Q_{rad} = C_{sca}/(C_{sca} + C_{abs})$, are presented at $\lambda = 820$ nm, as a function of the particle diameter. Data of dielectric functions is again taken from ref. [17], and expressions for the scattering and absorption cross sections from eqs. (2.35) and (2.36). As the transmission spectrum of the silver island film does not change considerably with increasing particle size, scattering properties of the island film alone cannot explain the increased photocurrent enhancement. Increase in the radiative efficiency of the particles is not sufficient to explain the observed behaviour either, as stated by Stuart and Hall [22].

Apparently, explanation lies in the properties of the coupled metal island-waveguide system: the scattering cross section of the metal islands for waveguided light is enhanced by the waveguide interaction much more than scattering cross section of the bare island film alone. The increase in the scattering efficiency of the bare island film could be multiplied as the energy in the guided modes of the SOI waveguide, once coupled in by the metal islands, is coupled back to the radiative modes of metal islands and then coupled again into the trapped modes in waveguide, and this process is repeated multiple times [20].

There, however, is a limit after which the increase in the particle size decreases the photocurrent enhancement due to multipole oscillations, which decrease scattering, as stated in chapter 3.1.3 [22]. The decrease in scattering efficiency means that smaller fraction of the radiation exciting the particle (either light incident from outside of the waveguide, or the electromagnetic modes in the waveguide) is emitted into the waveguide [21]. All in all, it is beneficial to maximize the radiative efficiency and scattering cross section of the metal island film to allow largest possible portion of light extincted by the particles to be coupled into the waveguide (as opposed to being absorbed). This suggests that silver is the optimal nanoparticle material for SOI cells, as it has very high radiative efficiency (see fig. 2.11).

4.1.4 Effect of waveguide width

Comparison of the photocurrent enhancement spectra in figs. 3.2(b), 3.3(a), 3.5(b), 3.7(a) and 3.11(a) shows change in position, number and shape of the enhancement peaks as the thickness of waveguide (active Si layer) changes. In first three figures, thickness of the active layer is 160 nm, 95 nm in 3.7(a) and 1250 nm in 3.11(a). The wider the waveguide, the more modes it can support, and the more enhancement peaks are observed. This supports the conclusion

that photocurrent enhancement peaks are related to trapped electromagnetic radiation modes supported by the waveguide.

4.1.5 Effect of dielectric environment and spacer layer

Altering the dielectric environment of metal particles shifts the LSP resonance wavelength. This is perceived for metal island films in refs. [12] and [27]. Shifting of the bare island resonance wavelength towards resonance wavelength of the coupled island-waveguide system is observed to produce an increase in the magnitude of the photocurrent enhancement peak corresponding to the resonance, as reported by Pillai *et al* [12](see fig. 3.7). In this case, redshift in the LSP resonance wavelength by dielectric overcoating also results in a redshift in the resonance peak of the coupled metal island-waveguide system. This is somewhat contrary to the observations in ref. [18], which indicate that that the position of the photocurrent enhancement peak remains unaltered when the wavelength of the bare island resonance changes. However, now the case is that the properties of the waveguide are also changed by the dielectric overcoating, as opposed to the particle size affecting only the particle resonance.

For increasing spacer layer thickness the number of peaks remains the same but peaks shift to longer wavelengths. Also, the peaks get weaker as the thickness increases beyond certain limit [19]. The decrease in peak magnitude arises from weakened coupling between the islands and the waveguide.

4.2 Nanoparticles on thin-film Si cells

Papers presented in section 3.3 [8, 24, 25] deal with gold nanoparticles deposited on silicon *pn* and *p-i-n* junction diodes. Apart from the lack of waveguide geometry, the main difference to the studies presented in sections 3.1 and 3.2 is the considerably lower particle density: density of the gold particles is roughly ten times smaller than the density of the metal islands deposited on the SOI devices. The particle shape is also more spherical and regular due to a different deposition method. Obtained photocurrent and photocurrent enhancement spectra are shown in figs. 3.16 and 3.21, revealing wide photocurrent enhancement peaks centered around the LSP resonance wavelength.

Without the waveguide properties of the SOI devices, photocurrent enhancement remains comparatively low. the largest observed photocurrent enhancement is 1.8 fold enhancement in fig. 3.16. Without the ability to support waveguided radiation modes, the main factor behind enhanced photocurrent is the electric field of the gold particles. This can be established from fig. 3.23, which
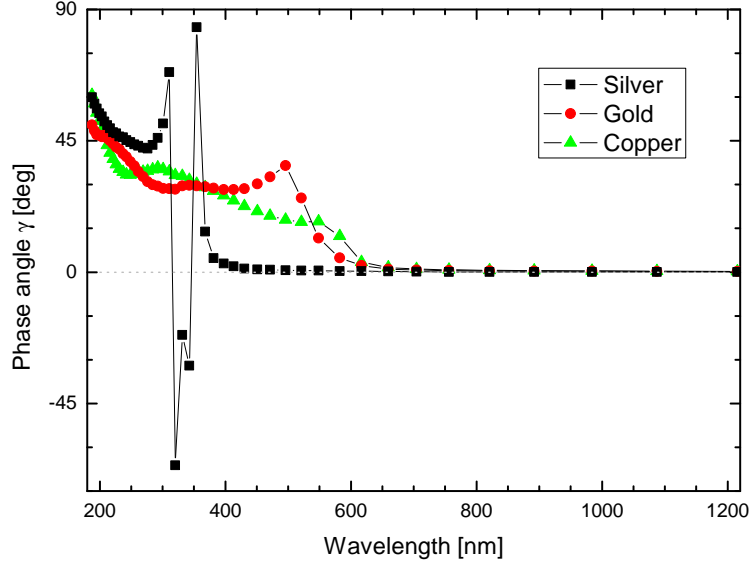
Figure 4.2: Phase angle γ of polarizability $\alpha = |\alpha|e^{i\gamma}$ of a spherical particle made of silver, gold and copper. Data of dielectric functions taken from ref. [17] and expression for polarizability from eq. (2.26).

shows simulated $|\mathbf{E}|^2$ integrated over the semiconductor volume as a function of wavelength. The shapes of the curves for different particle diameters follow the shapes of measured photocurrent enhancements in fig. 3.21. Both the radiative and the near field components of the electric field of the plasmon excitation now contribute to the electric field magnitude. Schaadt *et al* propose that it is not only the increased electric field amplitude that causes the photocurrent enhancement, but also the increased interaction time between the electric field and the semiconductor [24]. The interaction time is now determined by the lifetime of the LSP excitation on a nanoparticle, which is 5 to 10 times longer than the transit time of a photon through the region of the LSP near field [24].

Because the total field within the semiconductor is the superposition of the transmitted and scattered fields, a phase difference can result in effective decrease in the total electric field amplitude, caused by destructive interference. The electric field of an oscillating dipole (both the radiative field and near field) is proportional to polarizability of the particle, $\alpha = |\alpha|e^{i\gamma}$, where the phase difference is given by phase angle γ. Effect of the decreased electric field ampli-

tude due to the destructive interference is observed both in the experimental measurements (fig. 3.21) and in the simulations (fig. 3.23). In fig. 4.2 the phase angle of polarizability for spherical silver, gold and copper particles in air is presented as a function of wavelength. A non-zero phase difference can be observed for a gold particle at wavelengths shorter than 600 nm, which corresponds to the region of decreased photocurrent in fig. 3.21.

Derkacs *et al.* have simulated the effect of the particle density on the total electric field $|E|^2$ integrated over the volume of their a-Si:H test cell. The enhancement ratio compared to a device without added nanoparticles is shown as a function of particle density for light of $\lambda = 600$ nm in fig. 3.19, showing that there is an optimal particle density, where the enhancement is maximized. There is no experimental results for the effect of different particle densities on the photocurrent enhancement available in the references. Optimization of the particle density for a broad wavelength range can be considered essential for the efficiency enhancement. The experiments presented in the references may not show the full potential of the metal nanoparticles on thin-film silicon solar cells.

4.3   Silver island films on planar silicon solar cells

Scattering by metal island films can also considerably enhance photocurrent output of a thick, wafer based planar Si solar cell, as demonstrated by Pillai *et al.* [3](see chapter 3.2). Metal island layer, with suitable particle diameter, on top of a thick planar silicon solar cell causes an increase in photocurrent at wavelength range from roughly 500 nm to at least 1200 nm, as seen in fig. 3.11(b). Comparison to the absorptance enhancement in a metal island layer equipped Si wafer, presented in fig. 3.12(a), shows that the photocurrent enhancement arises from the increased optical absorption in the silicon. In thick solar cells – thickness of the devices in ref. [3] was $300 \ \mu$m – radiative part of the plasmonic field is dominant within the major part of the semiconductor volume (see fig. 4.3). The absolute value of the radiative (far) field component is, roughly estimated, 100 times greater than that of the near field at distances in order of hundreds of microns. The increased optical absorption can therefore be assumed to arise from the scattering by the metal islands into the silicon. Comparison of optical absorptance and photocurrent enhancement plots reveals that the silver islands effectively absorb wavelengths between roughly 300 and 400 nm, causing a reduction in photocurrent in the device [3]. This supports the suggestion that the reradiation (scattering) by the particles is the dominant process contributing into the performance enhancement of a thick
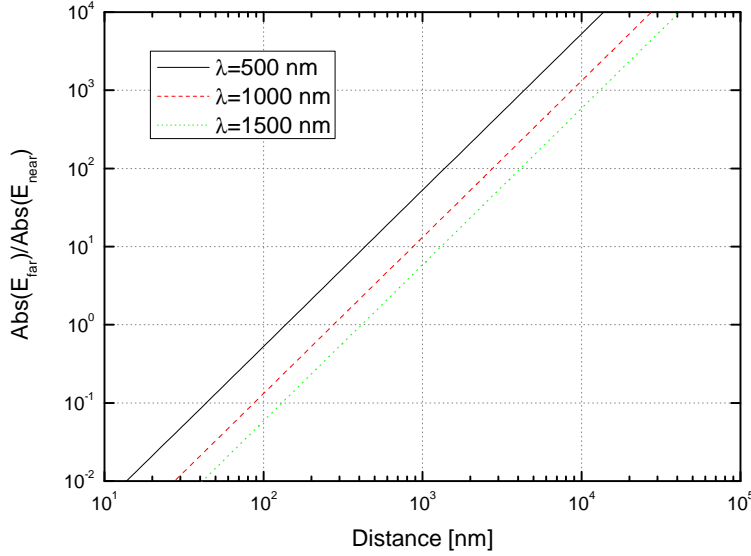
Figure 4.3: Relative amplitudes of the scattered and near electric field components of an oscillating point dipole. Expressions for electric fields taken from eq. 2.30.

solar cell, as opposed to the effect of the near field. The effective absorption in silver islands at $300 - 400$ nm wavelength could be due to the phase difference between transmitted and scattered electric fields at that wavelength region (see fig. 4.2), which results in destructive interference.

By comparing absorption (and photocurrent) enhancement spectrum to a reflectance spectrum it can be observed that, for thick solar cells, the metal island layer functions more like an antireflection coating at visible wavelengths (up to 1000 mn), whereas the effect of light trapping dominates at near infra-red wavelength range (above 1000 nm).

The largest photocurrent enhancement occurs at $1100 - 1200$ nm with the highest magnitude of $G \approx 7$. However, it should be brought to mind that this is the region of very weak absorption for silicon, and thus the enhancement does not convey the whole truth. The absolute photocurrent output, which in this regard would be very illustrative, is not presented in the reference. Moreover, the enhancement at the wavelength range of strong absorption of Si, from approx. 300 to 900 nm, cannot be clearly made out from the graph of the photocurrent enhancement spectra presented in fig. 3.11(b). Although the enhancement factor is just barely over unity in this range for all three curves presented, pho-

tocurrent enhancement at these wavelengths proves to be most crucial, as the highest total increase in photocurrent is achieved with Ag mass thickness with the lowest enhancement peak value (19% total increase with $G \approx 3$ peak for 12 nm Ag, see chapter 3.2). It can be observed, that it is not important whether the enhancement at wavelengths above 1000 nm is 3- or 7-fold, but what the enhancement over the wavelength range from 300 to 1000 nm is. It would be illustrative to examine the photocurrent enhancement spectrum more closely, but from fig. 3.11(b), the three photocurrent enhancement plots are indistinguishable from each other at this region of interest. This measurement by Pillai *et al.* should give a realistic representation of the effects of a metal island layer on a wafer based silicon solar cell performance, since the cell used here is an actual PERL cell, which has demonstrated a 24.7% efficiency [23].

4.3.1 Effect of particle size

In thick silicon wafers, effect of the increasing particle size is to increase the magnitude of the photocurrent enhancement peak at the long wavelength end of the spectrum (see figs. 3.11(b) and 3.12(a)). However, increasing particle size also seems to decrease photocurrent enhancement at the $400 - 1000$ nm wavelength range, which has a dramatic effect of overall photocurrent. In ref. [3], highest overall photocurrent enhancement is achieved with the smallest metal island layer thickness. Therefore, it is very important to optimize the island size and the thickness of the island layer in order to achieve optimal device performance.

4.4   Mechanisms behind the enhancements

It has been proposed by Kirkengen and Bergli [28] that the energy of localized surface plasmons on metal nanoparticles can create electron-hole pairs in silicon solar cells through two processes, which they call the indirect and direct absorption. In the indirect absorption, the energy of a plasmon is emitted by radiative electromagnetic fields (light) in directions along the semiconductor, increasing the effective optical path of the photons and thus increasing the probability of optical absorption. In case of an indirect band gap material, as with silicon, a phonon must be involved in the indirect absorption in order to preserve the conservation of momentum. In the direct absorption the near field of the plasmon excites electron-hole pairs into the semiconductor, and the conservation of momentum is preserved through a transfer of momentum to the metal particle.

The indirect absorption is clearly the dominant process in SOI structures with metal island layer, as the enhancements arise from the particles emitting energy into the propagating modes of the silicon waveguide. This process also dominates in the application of metal islands on thick planar cells. When the cell thickness is of the order of tens or hundreds of microns, the scattered field dominates over the near field in virtually all of the semiconductor volume. More surprisingly, based on the references discussed in this thesis, indirect absorption seems to dominate in thin-film silicon solar cells as well: in ref. [8] the photocurrent of a thin silicon diode is decreased at wavelengths where the scattered and transmitted fields interfere destructively, whereas the photocurrent output is increased at other wavelengths. However, this most probably arises from the placement of the particles in the experiments. Simulations in refs. [8] and [25] with gold particles deposited on top of a silicon junction diode show strongly enhanced electric field amplitude to the "left" of the particle. This is the near field of the particle: in eq. (2.31) the nominator $[(\hat{\mathbf{r}} \cdot \mathbf{p})\hat{\mathbf{r}} - \mathbf{p}]$ is minimized when $\hat{\mathbf{r}}$ is parallel to, and maximized when antiparallel to $\mathbf{p}$, where $\mathbf{p}$ is parallel to the direction of the electric field of the incident radiation, and perpendicular to the semiconductor surface. In short, this means that when the particles are deposited on top of the solar cell, the near field resides outside of the semiconductor volume. Therefore, in order to observe the effect of the direct carrier generation the metal particles would have to be deposited inside the semiconductor material and, preferably, near the junction depth.

Therefore, conclusions regarding the effect of the direct carrier generation by the near fields of metal particles cannot be made from the available references. According to Kirkengen and Bergli [28], the relative importance of the direct and indirect absorption (and losses to heat) as plasmon damping mechanisms depends on kr. (Here r is distance from the particle center and $k = 2\pi/\lambda$ the wave number.) With certain kr, the direct absorption dominates over the radiative damping. A 40% increase in absorptance in very thin film of (14 nm) a-Si due to embedded silver particles of 2.2 nm diameter has been reported by Mertens *et al.* [29] but, to our knowledge, this has not been studied with silicon junction diodes.

Chapter 5

Conclusions

For this thesis, a literature study on efficiency enhancement in three kinds of silicon solar cells by deposition of metal nanoparticles *on the front surface of the device* was carried out. These devices were traditional planar wafer based, thin-film silicon and silicon on insulator (SOI) solar cells. In the references, the efficiency of all three types of devices is enhanced by the deposition of metal nanoparticles. The quantity and quality of this enhancement may be adjusted with several parameters, such as the particle diameter, shape, density, material, the thickness of the separating spacer layer, the dielectric overcoating of the particles, etc. In all three kinds of devices, with metal nanoparticles deposited on the front surface of the device, the radiative (i.e. scattering) properties of the particles dominate over absorption. This may well be different for particles embedded into the semiconductor.

The waveguide geometry of SOI solar cells is optimal for exploitation of the radiative properties of the metal nanoparticles, demonstrating the largest enhancements: 36% increase in the total photocurrent output integrated over the AM1.5 solar spectrum [3]. The feasibility of manufacturing SOI type solar cells of polycrystalline [30, 31] and amorphous silicon with potential to a high efficiency enhancement with metal nanoparticles makes them a promising subject of further experiments and applications.

The efficiency of already high-efficient thick, planar solar cells is also enhanced by properties of the metal nanoparticles: a 16% total photocurrent enhancement integrated over the AM1.5 solar spectrum is demonstrated for a planar PERL type solar cell in ref. [3]. The metal nanoparticles provide enhanced photocurrent through light trapping at the wavelength region of poor absorption in silicon, the near infra-red, and act as an antireflection coating in the visible region.

An 8.1% increase in the total photocurrent output and 8.3% increase in the energy conversion efficiency due to the metal nanoparticles deposited on the device surface is demonstrated for a thin-film p-i-n type amorphous silicon solar cell in ref. [25]. Exploring the full potential of metal nanoparticles on thin-film solar cells would need thorough experimentation with different particle sizes and densities, as well as overcoatings on the particles and different spacer layer thicknesses and materials.

Experiments with metal nanoparticles embedded inside the semiconductor material, preferably near the junction depth, should be made in order to observe the near field effects on the direct charge carrier generation within silicon solar cells.

Bibliography

[1] N. S. Lewis. Toward cost-effective solar energy use. *Science*, 315:pp. 798–801, 2007.

[2] L. L. Kazmerski. Solar photovoltaics R&D at the tipping point: A 2005 technology overview. *Journal of Electron Spectroscopy and Related Phenomena*, 150:pp. 105–135, 2006.

[3] S. Pillai, K. R. Catchpole, T. Trupke, and M. A. Green. Surface plasmon enhanced silicon solar cells. *Journal of Applied Physics*, 101:p. 093105, 2007.

[4] M. A. Green. Recent developments in photovoltaics. *Solar Energy*, 76:pp. 3–8, 2004.

[5] A. V. Shah, H. Schade, M. Vanecek, J. Meier, E. Vallat-Sauvain, N. Wyrsch, U. Kroll, C. Droz, and J. Bailat. Thin-film silicon solar cell technology. *Progress in Photovoltaics: Research and Applications*, (12):pp. 113–142, 2004.

[6] M. A. Green, K. Emery, Y. Hishikawa, and W. Warta. Solar cell efficiency tables (version 31). *Progress in Photovoltaics: Research and Applications*, 16:pp. 61–67, 2008.

[7] Jenny Nelson. *The Physics of Solar Cells*. Imperial College Press, first edition, 2007.

[8] S. H. Lim, W. Mar, P. Mathieu, D. Derkacs, and E. T. Yu. Photocurrent spectroscopy of optical absorption enhancement in silicon photodiodes via scattering from surface plasmon polaritons in gold nanoparticles. *Journal of Applied Physics*, 101:p. 104309, 2007.

[9] Renewable Resource Data Center. Reference solar spectral irradiance: Air mass 1.5 — RReDC, 2008. [Online; retrieved October 3rd 2008].

[10] M. A. Green. Limiting efficiency of bulk and thin-film silicon solar cells in the presence of surface recombination. *Progress in Photovoltaics: Research and Applications*, 7:pp. 327–330, 1999.

[11] R. B. Bergmann and J. H. Werner. The future of crystalline silicon films on foreign substrates. *Thin Solid Films*, 403-404:pp. 162–169, 2002.

[12] S. Pillai, K. R. Catchpole, T. Trupke, G. Zhang, J. Zhao, and M. A. Green. Enhanced emission from si-based light-emitting diodes using surface plasmons. *Applied Physics Letters*, 88:p. 161102, 2006.

[13] C. F. Bohren and D. R. Huffman. *Absorption and Scattering of Light by Small Particles*. Wiley & Sons, Inc., 10th edition, 1998.

[14] C. F. Bohren. How can a particle absorb more than the light incident on it? *American Journal of Physics*, 51:pp. 323–327, 1983.

[15] Stefan Alexander Maier. *Plasmonics: Fundamentals and Applications*. Springer, first edition, 2007.

[16] A. V. Zayats, I. I. Smolyaninov, and A. A. Maradudin. Nano-optics of surface plasmon polaritons. *Physics Reports*, 408:pp. 131–314, 2005.

[17] P. B. Johnson and R. W. Christy. Optical constants of the noble metals. *Physical Review B*, 6(12):pp. 4370–4379, 1972.

[18] H. R. Stuart and D. G. Hall. Absorption enhancement in silicon-on-insulator waveguides using metal island films. *Applied Physics Letters*, 69(16):pp. 2327–2329, 1996.

[19] H. R. Stuart and D. G. Hall. Enhanced dipole-dipole interaction between elementary radiators near a surface. *Physical Review Letters*, 80(25):pp. 5663–5666, 1998.

[20] K. R. Catchpole and S. Pillai. Absorption enhancement due to scattering by dipoles into silicon waveguides. *Journal of Applied Physics*, 100:p. 044504, 2006.

[21] K. R. Catchpole and S. Pillai. Surface plasmons for enhanced silicon light-emitting diodes and solar cells. *Journal of Luminescence 121*, pages pp. 315–318, 2006.

[22] H. R. Stuart and D. G. Hall. Island size effects in nanoparticle-enhanced photodetectors. *Applied Physics Letters*, 73(26):pp. 3815–3817, 1998.

[23] J. Zhao, A. Wang, and M. A. Green. 24.7% efficiency silicon PERT cells on MCZ substrates and 24.7 % efficiency PERL cells on FZ substrates. *Progress in Photovoltaics: Research and Applications*, 7:pp. 471–474, 1999.

[24] D. M. Schaadt, B. Feng, and E. T. Yu. Enhanced semiconductor optical absorption via surface plasmon excitation in metal nanoparticles. *Applied Physics Letters*, 86:p. 063106, 2005.

[25] D. Derkacs, S. H. Lim, P. Mathieu, and E. T. Yu. Improved performance of amorphous silicon solar cells via scattering from surface plasmon polaritons in nearby metallic nanoparticles. *Applied Physics Letters*, 89:p. 093103, 2006.

[26] B. J. Soller and D. G. Hall. Energy transfer at optical frequencies to silicon-based waveguiding structures. *Journal of the Optical Society of America A*, 18(10):pp. 2577–2584, 2001.

[27] G. Xu, M. Tazawa, P. Jin, S. Nakao, and K. Yoshimura. Wavelength tuning of surface plasmon resonance using dielectric layers on silver island films. *Applied Physics Letters*, 82(22):pp. 3811–3813, 2003.

[28] M. Kirkengen, J. Bergli, and Y. M. Galperin. Direct generation of charge carriers in c-si solar cells due to embedded nanoparticles. *Journal of Applied Physics*, 102:p. 093713, 2007.

[29] H. Mertens, J. Verhoeven, A. Polman, and F. D. Tichelaar. Infrared surface plasmons in two-dimensional silver nanoparticle arrays in silicon. *Applied Physics Letters*, 85(8):pp. 1317–1319, 2004.

[30] S. Arimoto, H. Morikawa, M. Deguchi, Y. Kawama, Y. Matsuno, T. Ishihara, H. Kumabe, and T. Murotani. High efficient operation of large-area 100 cm2 thin film polycrystalline silicon solar cell based on SOI structure. *Solar Energy Materials and Solar Cells*, 34(1):pp. 257–262, 1994.

[31] H. Morikawa, Y. Nishimoto, H. Naomoto, Y. Kawama, A. Takami, and S. Arimoto. 16.0% efficiency of large area 10 cm x 10 cm thin film polycrystalline silicon solar cell. *Solar Energy Materials and Solar Cells*, 53(1):pp. 23–28, 1998.